LUND UNIVERSITY

Computational patient models for simulation of dynamic gamma-camera imaging

Application to renography and peptide receptor radionuclide therapy

Brolin, Gustav

2017

Document Version:
Publisher's PDF, also known as Version of record

Computational patient models for simulation of dynamic gamma-camera imaging

Application to renography and peptide receptor radionuclide therapy

GUSTAV BROLIN
FACULTY OF SCIENCE | LUND UNIVERSITY

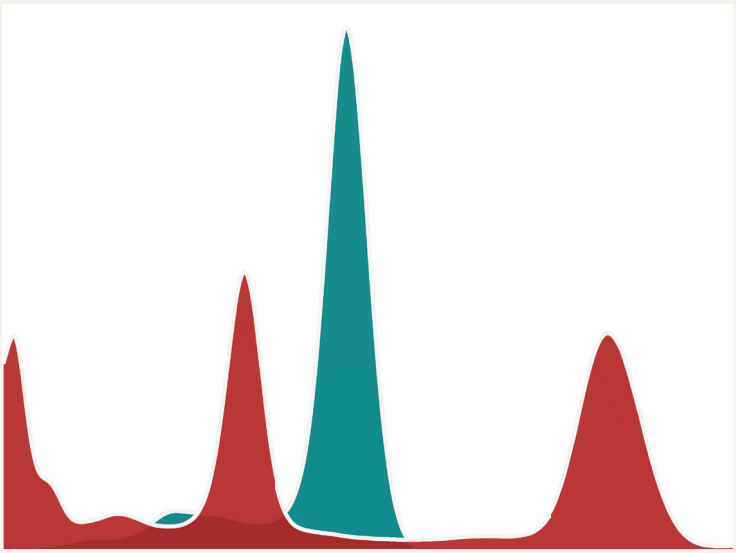

Computational patient models for simulation of dynamic gamma-camera imaging

Application to renography and peptide receptor radionuclide therapy

Computational patient models for simulation of dynamic gamma-camera imaging

Application to renography and peptide receptor radionuclide therapy

Gustav Brolin

LUND
UNIVERSITY

DOCTORAL DISSERTATION
by due permission of the Faculty of Science, Lund University, Sweden.
To be defended on Friday the 6th of October 2017, 09:00, at lecture hall F3, Skåne University Hospital, Lund.

Thesis advisors

Michael Ljungberg and Katarina Sjögreen Gleisner

Faculty opponent

Manuel Bardiés, Research Director, Cancer Research Center, Toulouse, France

Organisation LUND UNIVERSITY Department of Medical Radiation Physics Skåne University Hospital, Lund SE-221 58 Lund, Sweden	Document name DOCTORAL DISSERTATION Date of issue 2017-10-06
Author(s) Gustav Brolin	Sponsoring organisation

Title and subtitle

Computational patient models for simulation of dynamic gamma-camera imaging

Application to renography and peptide receptor radionuclide therapy

Many nuclear medicine investigations rely on gamma-camera imaging to study and quantify the distribution of radiopharmaceuticals or radionuclides in the patient as a function of time. This is typically used for diagnostic studies of physiological functions or for calculation of absorbed doses following radionuclide therapy. In this work, computational patient models (phantoms) have been developed and used for evaluation of quantitative methods and techniques relying on dynamic gamma-camera imaging.

Papers I and II concern ^{99m}Tc-MAG3 dynamic renography, a well-established diagnostic modality for evaluation of renal function. In paper I, a patient model featuring the pharmacokinetics of ^{99m}Tc-MAG3 was presented. The developed framework readily allows modelling of various cases of clinical interest in a systematic manner. Dynamic image acquisition was simulated using the Monte Carlo method, and the resulting image data were encapsulated in the DICOM format to allow processing with software used in clinical practice. In paper II, this data were used to investigate the accuracy and inter-departmental variability in dynamic renography analysis, with participation from 21 nuclear medicine departments in Sweden. We found that the variability in estimates of renal TAC parameters is low and acceptable when renal function is normal, but considerably high when renal function is impaired. The accuracy of relative uptake measurements was negatively affected by the lack of attenuation correction for quantitation.

Papers III-IV concern image-based, patient-specific dosimetry in peptide receptor radionuclide therapy (PRRT) with ^{177}Lu-DOTATATE. Paper III describes the development of computational patient models for research on image-based dosimetry, based on the same approach as used in paper I. A preliminary evaluation of a realistic dosimetry protocol, based on a single SPECT and four planar scans, was performed and it was shown that absorbed doses to organs and tumours were accurate within ±25 %. In paper IV, the patient models were used in a thorough analysis of uncertainty in renal dosimetry based entirely on SPECT/CT, and a total uncertainty of approximately 6 % (1 standard deviation) was estimated in the absorbed dose to the kidneys. In paper V, the dosimetric impact of the long-lived meta-stable isomer ^{177m}Lu was studied. Furthermore, it was investigated if current dosimetry protocols, relying on measurements limited to the first week after treatment, are sufficient to predict the long-term activity retention. The results showed a negligible contribution from ^{177m}Lu to the whole-body absorbed dose, and that measurements performed more than one week after treatment are warranted for tumour and whole-body dosimetry.

In conclusion, this thesis provides a contribution to the knowledge of measurement accuracy and uncertainty in dynamic renography and ^{177}Lu PRRT.

Key words

Nuclear medicine, Gamma camera, Renography, Radionuclide therapy, Pharmacokinetics, Internal dosimetry

Classification system and/or index terms (if any)

Supplementary bibliographical information		Language English
ISSN and key title		ISBN 978-91-7753-385-6 (print) 978-91-7753-386-3 (pdf)
Recipient's notes	Number of pages 86	Price
	Security classification	

Signature 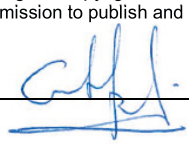 Date 2017-08-24

Computational patient models for simulation of dynamic gamma-camera imaging

Application to renography and peptide receptor radionuclide therapy

Gustav Brolin

LUND
UNIVERSITY

Cover illustration: ^{99m}Tc and ^{177}Lu energy spectra from a gamma camera

Faculty of Science | Department of Medical Radiation Physics

ISBN
978-91-7753-385-6 (print)
978-91-7753-386-3 (pdf)

Printed in Sweden by Media-Tryck, Lund University
Lund 2017

Content

List of abbreviations

2D	Two-dimensional
3D	Three-dimensional
BED	Biologically Effective Dose
CPS	Counts per second
CT	(X-ray) Computed Tomography
DOTATATE	Dota-octreotate
FBP	Filtered back-projection
MAG3	Mercapto-acetyl-tri-glycine
PET	Positron Emission Tomography
PK	Pharmacokinetic
PRRT	Peptide Receptor Radionuclide Therapy
PVE	Partial Volume Effect
RNP	Radionuclide Purity
RNT	Radionuclide Therapy
ROI	Region-of-Interest (2D)
RRF	Relative Renal Function
SPECT	Single Photon Emission Tomography
TAC	Time-activity Curve
VOI	Volume-of-Interest (3D)

List of original papers

This thesis is based on the following papers, henceforth referred to by their Roman numerals:

I **Dynamic ^{99m}Tc-MAG3 renography: images for quality control obtained by combining pharmacokinetic modelling, an anthropomorphic computer phantom and Monte Carlo simulated gamma camera imaging**

Gustav Brolin, Katarina Sjögreen Gleisner, and Michael Ljungberg
Physics in Medicine and Biology, 2013. **58**, pp. 3145 – 3161

II **The accuracy of quantitative parameters in ^{99m}Tc-MAG3 dynamic renography: A national audit based on virtual image data**

Gustav Brolin, Lars Edenbrandt, Göran Granerus, Anna Olsson, David Afzelius, Agneta Gustafsson, Cathrine Jonsson, Jessica Hagerman, Lena Johansson, Katrine Åhlström Riklund, and Michael Ljungberg
Clinical Physiology and Functional Imaging, 2016. **36**, pp. 146 – 154

III **Pharmacokinetic digital phantoms for accuracy assessment of image-based dosimetry in ^{177}Lu-DOTATATE peptide receptor radionuclide therapy**

Gustav Brolin, Johan Gustafsson, Michael Ljungberg, and Katarina Sjögreen Gleisner
Physics in Medicine and Biology, 2015. **60**, pp. 6131 – 6419

IV **Uncertainty propagation for SPECT/CT-based renal dosimetry in ^{177}Lu peptide receptor radionuclide therapy**

Johan Gustafsson, **Gustav Brolin**, Maurice Cox, Michael Ljungberg, Lena Johansson, and Katarina Sjögreen Gleisner
Physics in Medicine and Biology, 2015. **60**, pp. 8329 – 8346

V **Long-Term Retention of ^{177}Lu/^{177m}Lu-DOTATATE in Patients Investigated by γ-Spectrometry and γ-Camera Imaging**

Katarina Sjögreen Gleisner, **Gustav Brolin**, Anna Sundlöv, Edita Mjekiqi, Karl Östlund, Jan Tenvall, and Erik Larsson
Journal of Nuclear Medicine, 2015. **56**, pp. 976 – 984

Copyright statements

Paper I

https://doi.org/10.1088/0031-9155/58/10/3145

Paper II

https://doi.org/10.1111/cpf.12208

Paper III

https://doi.org/10.1088/0031-9155/60/15/6131

Paper IV

https://doi.org/10.1088/0031-9155/60/21/8329

Paper V

https://doi.org/10.2967/jnumed.115.155390

List of contributions

Paper I

I developed the kinetic model and computer code for generating the time-activity curves. I performed the simulations, and authored the manuscript.

Paper II

I participated in the case design and generated the phantoms with time-activity curves for the simulations. I analysed the results and authored the manuscript.

Paper III

I participated in the data collection, and developed the phantoms including the pharmacokinetic model. I was the main author of the manuscript.

Paper IV

I participated in the planning of the study, and provided the computer phantoms used in the Monte Carlo-experiments. I participated in the preparation of the physical phantom and in the SPECT acquisitions. I reviewed and commented on the manuscript.

Paper V

I participated in the collection of patient data and in the compilation of decay data for ^{177m}Lu/^{177}Lu. I designed one figure and participated in the writing of the manuscript.

Abstract

Many nuclear medicine investigations rely on gamma-camera imaging to study and quantify the distribution of radiopharmaceuticals or radionuclides in the patient as a function of time. This is typically used for diagnostic studies of physiological functions or for calculation of absorbed doses following radionuclide therapy. In this work, computational patient models (phantoms) have been developed and used for evaluation of quantitative methods and techniques relying on dynamic gamma-camera imaging.

Papers I and II concern ^{99m}Tc-MAG3 dynamic renography, a well-established diagnostic modality for evaluation of renal function. In paper I, a patient model featuring the pharmacokinetics of ^{99m}Tc-MAG3 was presented. The developed framework readily allows modelling of various cases of clinical interest in a systematic manner. Dynamic image acquisition was simulated using the Monte Carlo method, and the resulting image data were encapsulated in the DICOM format to allow processing with software used in clinical practice. In paper II, this data were used to investigate the accuracy and inter-departmental variability in dynamic renography analysis, with participation from 21 nuclear medicine departments in Sweden. We found that the variability in estimates of renal TAC parameters is low and acceptable when renal function is normal, but considerably high when renal function is impaired. The accuracy of relative uptake measurements was negatively affected by the lack of attenuation correction for quantitation.

Papers III-IV concern image-based, patient-specific dosimetry in peptide receptor radionuclide therapy (PRRT) with ^{177}Lu-DOTATATE. Paper III describes the development of computational patient models for research on image-based dosimetry, based on the same approach as used in paper I. A preliminary evaluation of a realistic dosimetry protocol, based on a single SPECT and four planar scans, was performed and it was shown that absorbed doses to organs and tumours were accurate within ±25 %. In paper IV, the patient models were used in a thorough analysis of uncertainty in renal dosimetry based entirely on SPECT/CT, and a total uncertainty of approximately 6 % (1 standard deviation) was estimated in the absorbed dose to the kidneys. In paper V, the dosimetric impact of the long-lived meta-stable isomer ^{177m}Lu was studied. Furthermore, it was investigated if current dosimetry protocols, relying on measurements limited to the first week after treatment, are sufficient to predict the long-term activity retention. The results showed a negligible contribution from ^{177m}Lu to the whole-body absorbed dose, and that measurements performed more than one week after treatment are warranted for tumour and whole-body dosimetry.

In conclusion, this thesis provides a contribution to the knowledge of measurement accuracy and uncertainty in dynamic renography and ^{177}Lu PRRT.

Populärvetenskaplig sammanfattning

Inom nuklearmedicinen utnyttjas radioaktiva läkemedel och strålningen som sänds ut från dessa för att diagnosticera och behandla ett flertal olika sjukdomar. Det radioaktiva läkemedlet ges ofta till patienten som en intravenös injektion, och läkemedlets egenskaper i kombination med patientens fysiologi och eventuella sjukdom avgör hur läkemedlet sedan fördelas, omsätts och utsöndras från kroppen. Denna dynamiska process kan följas med hjälp av en gammakamera (scintillationskamera) som genom att detektera strålningen från det radioaktiva ämnet skapar en bild av aktivitetsfördelningen i kroppen vid olika tidpunkter efter injektionen.

Det är i många sammanhang av intresse att använda den nuklearmedicinska bilden för att beräkna hur mycket av läkemedlet eller radionukliden som tagits upp i t.ex. ett organ eller tumör som funktion av tiden efter injektionen. Ett sådant sammanhang är vid renografi, en typ av njurundersökning där upptaget och utsöndringen av det radioaktiva läkemedlet avspeglar njurarnas funktion. Ett annat sådant sammanhang är vid radionuklidterapi, det vill säga behandling av cancer eller andra sjukdomar med radioaktiva läkemedel. Inom radionuklidterapi kan mätvärdena användas för att beräkna stråldoser till tumörer och friska organ. Stråldoserna avgör sedan hur mycket av det radioaktiva läkemedlet som ska ges till patienten för att maximera behandlingseffekten utan att risken för strålskador på friska organ blir oacceptabelt hög.

Det är ur ett patientsäkerhetsperspektiv givetvis av största betydelse att de mät- och beräkningsmetoder som används i dessa sammanhang ger tillförlitliga resultat, och att de mätosäkerheter och begränsningar som finns blir noggrant utredda. I detta arbete har vi undersökt tillförligheten i mätvärden som tas fram vid renografi med det radioaktiva läkemedlet ^{99m}Tc-MAG3 samt i stråldosberäkningar vid radionuklidterapi med ^{177}Lu-DOTATATE. Detta har dels gjort med konventionella mätningar, men främst genom datorexperiment med digitala patientmodeller. Patientmodellerna har konstruerats med hjälp av befintliga datormodeller av den mänskliga anatomin i kombination med framtagna farmakokinetiska modeller, vilka beskriver hur läkemedlet fördelar sig i kroppen som funktion av tiden efter injektion. Datorsimulering av gammakamerabildtagning med dessa patientmodeller ger bilder som är mycket patientlika och har visat sig vara användbara för utredning av osäkerheter och mätnoggrannhet, vilket i förlängningen kan bidra till bättre nuklearmedicinsk diagnostik och förbättrade behandlingsresultat vid radionuklidterapi.

1. Aim

The aim of the work presented in this thesis has been to increase the knowledge of the quantitative performance, uncertainties, and limitations of ^{99m}Tc-MAG3 renography and ^{177}Lu PRRT dosimetry. This aim has primarily been pursued by development and application of computational patient models (phantoms), focussing on modelling the kinetic properties of the above mentioned radiopharmaceuticals, and computer simulations of dynamic gamma-camera imaging using the Monte Carlo method. The specific aims of the studies included in this thesis were:

- to develop representative computational patient models and simulated datasets for ^{99m}Tc-MAG3 dynamic renography (paper I), for use in a national audit on the clinical accuracy and inter-hospital variability of the diagnostic method (paper II),
- to develop computational models of patients receiving radionuclide therapy with ^{177}Lu-DOTATATE (paper III),
- to perform error propagation and uncertainty estimation in patient-specific image-based dosimetry (paper IV) using the ^{177}Lu-DOTATATE patient models from paper III, and
- to investigate the dosimetric impact of long-term activity retention and radionuclide impurities in ^{177}Lu-DOTATATE PRRT dosimetry (paper V).

2. Introduction

Nuclear medicine

Approximately 110 000 diagnostic and therapeutic nuclear medicine procedures are performed at Swedish hospitals each year (2015 [1]). In most diagnostic and in some therapeutic applications, the administration of a radiopharmaceutical is followed by imaging to study the *in vivo* distribution of the injected radiopharmaceutical. There are two radiopharmaceutical-imaging devices that are in widespread clinical use: gamma cameras (chapter 3), which utilise single-photon emission and decay positioning by physical photon collimation; and positron emission tomography (PET) cameras, which utilise coincidence detection of annihilation radiation for positron decay positioning. Prototypes of both these devices were invented around the 1950s, but their clinical implementation timescales were quite different. In Sweden, the first commercial gamma camera was installed in already in 1967, and today about 100 systems can be found at both regional and university hospitals throughout the country [2]. By contrast, the first commercial PET system was installed in 1981 and the number of installed systems was only 12 as of 2014 [3]. The widespread routine clinical usage of PET did not occur until the beginning of the 2000s, and PET studies are still, to this date, almost exclusively performed at the university hospitals. However, an expansion of this technique to the regional hospitals has recently been initiated; the first PET system at a Swedish regional hospital was installed in 2014 and more will follow in the years to come.

The early adoption of the gamma camera as standard clinical equipment can be attributed to the invention of the ^{99m}Tc generator in 1958 [4] and the development of kit formulations for synthesis of ^{99m}Tc-labeled radiopharmaceuticals [5]. As shown in figure 1, the use of ^{99m}Tc is slowly decreasing, but still today constitutes approximately 75 % of all radionuclide administrations at Swedish hospitals. The applications are numerous and include studies of lung ventilation and perfusion [6], myocardial perfusion [7], and renal function (further discussed below).

The introduction of PET cameras as a widespread clinical modality was slowed down by the lack of an isotope with availability and labelling possibilities similar to ^{99m}Tc. The production of PET radiopharmaceuticals does in general require a nearby cyclotron and radiochemistry facility, owing to the short half-life of most common positron-emitting radionuclides. However, the number of cyclotrons for production

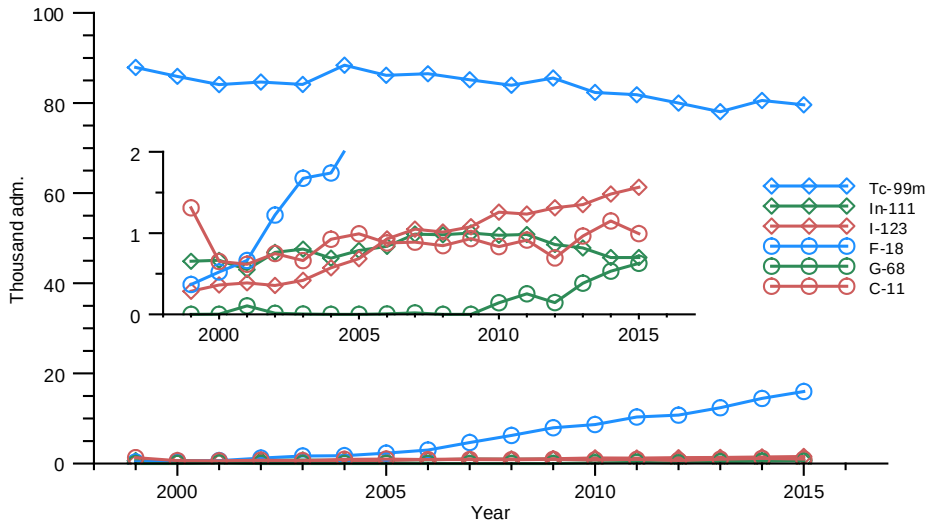

Figure 1. Number (of thousands) of administrations of various radionuclides for PET (circles) and gamma-camera (diamonds) studies per year at Swedish hospitals between 1999 and 2015 [1]. The most prominent trend is the steady increase in the number of ^{18}F PET studies beginning around 2005, and the slow but steady decrease in ^{99m}Tc studies.

of PET isotopes is steadily increasing, as are the number of PET scans conducted each year. The majority of PET scans are dedicated to oncology, using the glucose analogue ^{18}F-FDG (fluoro-deoxy-glucose) for tumour localisation and disease staging. ^{18}F has a half-life of 110 min and is produced by proton-bombardment of ^{18}O-enriched water. The annual number of FDG studies performed in Sweden is currently increasing at a rate exceeding 10 % a year [1]. Although there are several other radionuclides suitable for PET, such as ^{68}Ga, ^{11}C, and ^{13}N, and a large interest in the PET research community for other radiopharmaceuticals, ^{18}F will likely be the most commonly used PET radionuclide for many years to come.

In diagnostic nuclear medicine, the amount of activity administered to the patients is too low to produce any detectable biological effect resulting from the irradiation. In therapeutic nuclear medicine, also known as radionuclide therapy (RNT), the activity is administered with the intent of inducing such an effect in the targeted organ or tissue, which in general requires a higher amount of activity or radionuclides with a higher yield of charged-particle emissions. By proper design of the targeting agent and choice of radionuclide, it is possible to effectively irradiate a specific target while keeping the absorbed dose to other tissues and organs at a tolerable level. In 2015, approximately 3900 radionuclide therapies were given at Swedish hospitals. Of these, 2100 were treatments of hyperthyroidism and thyroid cancer using ^{131}I (NaI). The high prevalence of this type of treatment can be partly

explained by the targeting properties of the radioactive iodine ions. The natural uptake and accumulation of iodine in the thyroid means that no radiolabelling of a targeting agent is required. A similar "simple" targeting technique is exploited for palliative treatment of prostate cancer skeletal metastases with ^{223}Ra (RaCl). ^{223}Ra is an alpha-emitter that accumulates in skeletal bone due to its chemical similarity to calcium, and the short-range alpha particles from ^{223}Ra effectively irradiate skeletal metastases while sparing the bone marrow. The number of ^{223}Ra treatments administered at Swedish hospitals is at present increasing dramatically, from only 38 in 2005 to almost 1200 in 2015.

Dynamic renal scintigraphy

Dynamic renal scintigraphy, or renography for short, is a common diagnostic nuclear medicine technique for evaluating renal function and diagnosing renovascular hypertension and obstructive uropathy [8]. The study relies on an intravenous bolus injection of a radiopharmaceutical that is rapidly cleared from the body by glomerular filtration or tubular secretion in the kidneys.

After injection, the distribution and elimination of the radiopharmaceutical is followed by means of dynamic gamma-camera imaging, to visualise the time-course of renal uptake and excretion on a frame-by-frame basis. The image acquisition is normally performed in 10- or 20-s frames during approximately 30 min, with a single camera head acquiring planar projections from a posterior position. Figure 2 shows example ^{99m}Tc-MAG3 image data between zero and ten min post-injection, from a patient with normal renal function and from a patient with high-grade chronic kidney disease (CKD) [9]. In the patient with normal renal function, there is a rapid uptake of activity in the kidneys and subsequent excretion into the urinary bladder, accompanied by a decrease of background (non-renal) activity. The blood clearance and excretion is much slower in the patient with CKD, resulting in a lower kidney-to-background signal ratio and clear visualisation of blood pool activity in the heart, liver, and spleen.

Dynamic renal scintigraphy is further discussed in chapter 8.

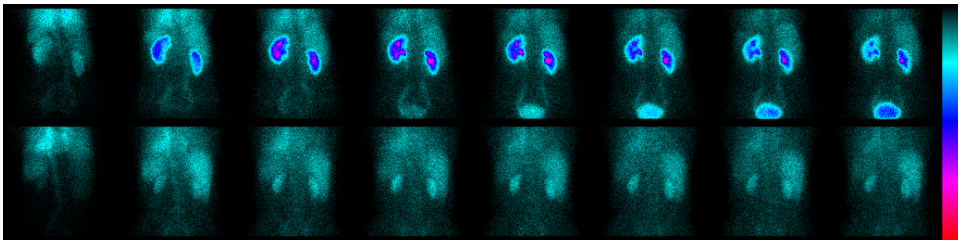

Figure 2. ^{99m}Tc-MAG3 dynamic renography data from a patient with normal renal function (top row) and from a patient with impaired renal function (bottom row). Each frame corresponds to 60 s of acquisition and should be viewed from left-to-right. Renography studies downloaded from the *database of dynamic renal scintigraphy* [9].

Peptide receptor radionuclide therapy

Peptide receptor radionuclide therapy (PRRT) is an increasingly used form of RNT for treatment of disseminated tumours of neuroendocrine origin. The therapeutic modality evolved from a diagnostic method for gamma-camera imaging of somatostatin-receptor positive tumours using ^{123}I-Octreotide [10] and later ^{111}In-DTPA-Octreotide [11, 12]. It was hypothesised that ^{111}In-DTPA-Octreotide could be useful also as a therapeutic agent, considering that the targeting mechanism, i.e., receptor-based internalisation, in combination with the short-range Auger and conversion electrons emitted in the decay of ^{111}In, could selectively irradiate somatostatin-receptor positive tumour cells [13]. Initial studies were conducted with modest results, and efforts were undertaken to develop compounds labelled with ^{90}Y and ^{177}Lu, based on the hypothesis of increased efficacy due to the longer range and tissue penetration of the beta particles emitted in the radioactive decay of these nuclei [14]. ^{177}Lu is particularly attractive for RNT, because, in addition to the beta particles, it also features gamma emissions at 113 keV and 208 keV that are suitable for gamma-camera imaging (see decay scheme in figure 15). To date, the most extensively used and studied radiopharmaceuticals for PRRT are ^{90}Y-Dota-Octreotide (DOTATOC) and ^{177}Lu-Dota-Octreotate (DOTATATE) [15, 16]. In Sweden, ^{177}Lu-DOTATATE is administered for PRRT, with approximately 3000 treatment sessions performed at the university hospitals in Uppsala, Gothenburg and Lund since first use in 2005 [1].

For patients with disseminated neuroendocrine tumours, PRRT is a well-tolerated treatment [15] with proven effects in terms of progression-free and overall survival [17]. The most significant adverse side-effects are hematologic toxicity and long-term nephrotoxicity due to irradiation of the kidneys and bone marrow [18, 19]. Many treatments are given using a conservative approach with four administrations of 7400 MBq. At this level of activity, toxicity is improbable [17].

On the assumption that higher amounts of activity, and thereby higher tumour absorbed doses, increases treatment efficacy, and that there is a dose-response relationship with regards to hematologic and renal toxicity [20], the standard dosage regimen is most likely too conservative for many patients, considering that the activity uptake and retention in normal organs varies considerably from patient to patient. This observation has motivated patient-specific treatment protocols guided by results from dosimetry based on quantitative gamma-camera imaging performed during the treatment course. Dosimetry in PRRT with ^{177}Lu-DOTATATE is further discussed in chapter 9.

3. The gamma camera

The gamma camera was invented by Hal Anger already in the 1950's [21], but the principal design, major components, and theory of operations are essentially unchanged in the majority of modern cameras found at nuclear medicine departments today. Although new camera technology based on semiconductor detectors (Cadmium-Zink-Telluride) has recently emerged as an alternative for commercial general-purpose cameras [22] as well as in systems dedicated for myocardial perfusion SPECT [23, 24], the traditional technology remains largely unchallenged.

The major components of the conventional gamma camera, illustrated in figure 3, include a Pb parallel-hole collimator, a NaI(Tl) scintillation crystal, photomultiplier tubes (PMTs), associated pulse-processing electronics, and computer equipment. A photon that is transmitted through the collimator and absorbed in the scintillation crystal produces a scintillation, i.e., a small flash of optical light. NaI(Tl) has a high light yield compared to many other scintillators; the absorption of a 1 MeV photon generates about 40 000 scintillation photons in the wavelength range between 325 and 550 nm [25], well suited for efficient detection by PMTs. An array of PMTs coupled to the crystal converts the light into electrical pulses that are subsequently amplified and processed by electronic circuitry, analogue-digital converters, and computers. The use of multiple PMTs in a geometric array enables determination of the point of interaction in the crystal, by utilising the signal contributions from several PMTs in known positions in relation to the total signal generated by the single photon absorption. The gamma-camera image is formed by the spatial distribution of the interaction points in the crystal. As the total signal from all PMTs is proportional to the total energy released in the crystal, the system can be calibrated for measurement of the photon energy.

The collimator acts as a filter that selectively absorbs or transmits photons depending on their direction when impinging on the collimator surface, making it possible to infer the possible positions from which the photon originated. Most clinical gamma-cameras are equipped with parallel-hole collimators, which only transmit photons that have an angle of incidence approximately normal to the collimator face (type-1 event in figure 3). Consequently, the inferred emission position of a photon will lie somewhere along a straight line from the point of interaction in the crystal, perpendicular to the collimator face. Most photons with a larger angle of incidence will be absorbed in the collimator (type-2 event). The

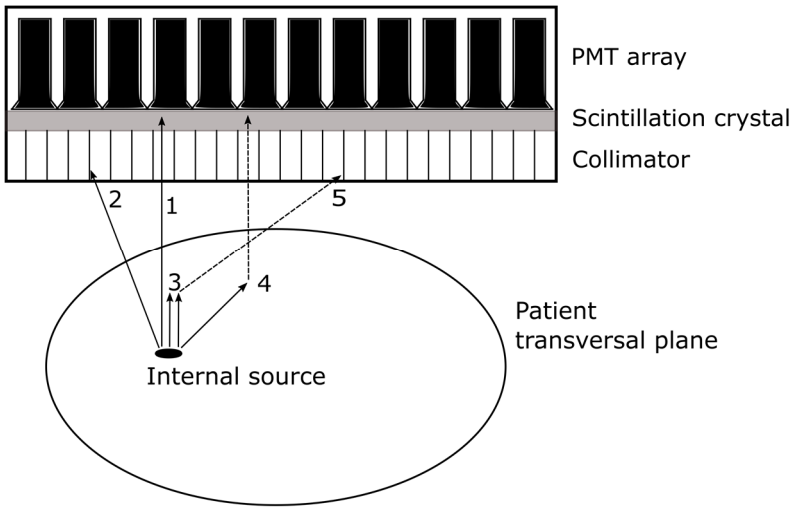

Figure 3. Schematic illustration of the gamma-camera and imaging process. The basic components of a traditional clinical camera system are a Pb parallel-hole collimator, an NaI(Tl) scintillation crystal, and an array of photomultiplier tubes (PMTs). Photons originating from a source in a patient may be transmitted through the collimator and absorbed in the crystal (1), be absorbed in the collimator if the angle if incidence exceeds the acceptance angle (2), and interact in the patient by photoelectric absorption or Compton scattering (3), with (4) or without (5) detection of a potential secondary scatter photon.

resulting image will thus approximately reflect the emission intensity, and thereby also the distribution of activity, in the plane co-aligned with the collimator face. The third dimension, the depth, remains unresolved as there is no intrinsic means to discriminate between two photons that have been detected at the same position but are originating from different depths in the patient. Therefore, the native gamma-camera image can to a first approximation be seen as a two-dimensional (2D) planar projection of the three-dimensional (3D) activity distribution in the patient.

Gamma-camera imaging can be performed either in planar or tomographic mode. In planar mode, the detector head is kept at a fixed angle during image acquisition, producing a single 2D projection image resulting from the true 3D activity distribution in the patient. In tomographic mode, commonly referred to as SPECT (Single Photon Emission Computed Tomography), the detector is rotated around the patient in order to acquire planar projection data from multiple angles. Using a suitable mathematical model for the imaging process, the set of 2D projections can be used to reconstruct tomographic images (“slices”) that together form an estimate of the activity distribution in 3D. SPECT is often aided by an X-ray computed tomography (CT) scan performed in direct conjunction to the SPECT scan. The CT data is useful for attenuation correction and provides an anatomical reference for the SPECT image as shown in figure 4. SPECT is preferable to planar

imaging in many circumstances, as it resolves the activity distribution in 3D. The main advantage with planar imaging over SPECT is speed, which thus allows for reasonable scanning times even for whole-body imaging, and that it generates less image data to process.

Modern general-purpose gamma cameras are often equipped with two detector heads capable of simultaneous acquisition of two opposing or perpendicular projection images, thus shortening the required imaging time. The gamma camera is often integrated with an X-ray CT in a combined SPECT/CT system, so that both SPECT and CT data may be acquired without the need to reposition the patient in-between the scans.

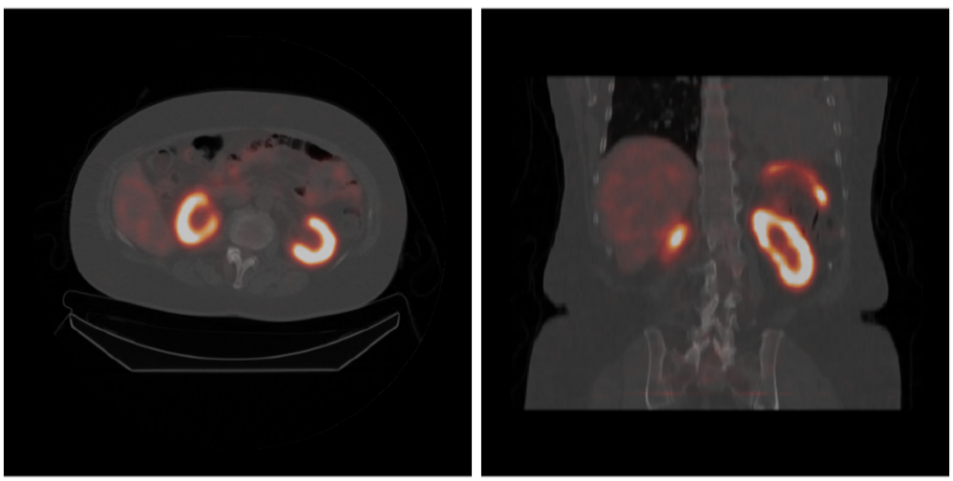

Figure 4. Example of a fused SPECT/CT image, showed as a transversal (left) and coronal (right) cross-section. The CT image (greyscale) provides an anatomical reference for the SPECT image (hot metal colour scale), here showing ^{177}Lu activity uptake in the kidneys, liver, and spleen.

Calibration and quantitative imaging

Although most gamma-camera studies are only qualitative or semi-quantitative at best, it is possible to perform quantitative imaging to determine the activity content or activity concentration of different organs and tissues. A key parameter in activity measurements with the gamma camera is the system sensitivity; a radionuclide- and camera-specific scalar value that relates a measured count rate in a calibration geometry to a known amount of activity. The sensitivity is commonly quoted in counts per second (cps) per MBq (cps/MBq) and is often measured free in air with a point- or disk-like source in the absence of any attenuating material. The system sensitivity for a gamma camera with a parallel-hole collimator is independent of source-collimator distance, which simplifies quantitative measurements since no correction for the source-detector distance is required. It is important to verify that the sensitivity is in fact constant and does not exhibit drift and day-to-day variations or a non-linear relationship between source activity and observed count rate. The former can be handled by regular gamma-camera quality control and tuning procedures, whereas the latter may require explicit dead-time correction for activity-quantification in high count-rate applications [26].

In its simplest form, activity quantification in a 2D gamma-camera image is performed by defining an image region-of-interest (ROI) encompassing the 2D projection of the source, counting the number of recorded pulses within the ROI per unit time, and dividing the result by the system sensitivity. However, several physical effects related to the image-formation process affect the measured count-rate and spatial distribution of the detected counts in a patient measurement, as compared to the calibration measurement. One such effect is the interaction of the emitted photons in the patient tissue, as schematically illustrated in figure 3. Photon attenuation (type-3 event in figure 3) – primarily by Compton scattering in the energy range around 100-200 keV, assuming atomic composition of soft tissue [27] – reduces the measured count rate per unit activity. The magnitude of the decrease is significant in most quantitative measurements, but depends on the location of the source within the patient. Photon attenuation is, to a small extent, counterbalanced by “scatter”, i.e., photons that originate from Compton interactions in the patient and where the scattering angle allow them to be transmitted through the collimator (type-4 event). However, scattered photons do not carry correct information regarding the distribution of activity because they originate from the scattering site and not from the site of the radioactive decay. By acquiring the image using an energy acceptance window, it is to some extent possible to discriminate against scattered photons since their energy is lower than the primary photons. However, the poor energy resolution of NaI(Tl)-based cameras does not allow perfect discrimination, meaning that there will always be a scatter contribution in the measured image.

The following two subsections outline the methodology of activity measurements using planar gamma-camera imaging and SPECT.

Planar activity quantification

If the position of the source in the patient is known, the activity in a region-of-interest (ROI) can be estimated from a single projection. The formation of a straight-parallel projection image $p(x,y)$ of a 3D activity distribution $f(x,y,z)$ along the z-axis is given by

$$p(x,y) = \varepsilon_{\text{air}} \cdot \int_{z_{min}(x,y)}^{z_{max}(x,y)} f(x,y,z) \exp\left[- \int_{z}^{z_{\max}(x,y)} \mu(x,y,z')dz' \right] dz \ , \qquad (1)$$

where ε_{air} is the system sensitivity in air, $\mu(x,y,z)$ is the distribution of linear attenuation coefficients – determined by the primary photon energy and the mass density and atomic composition of the tissue – and z_{min}, z_{max} are the patient boundary coordinates on the z-axis for a given coordinate (x,y). From equation (1), it is possible to derive an expression for the count rate R in a ROI according to (see appendix 1):

$$R = \iint_{ROI} p(x,y)dxdy = \varepsilon_{\text{air}} \cdot A_{ROI} \cdot e^{-\mu d} \ , \qquad (2)$$

where A_{ROI} is the ROI activity, i.e., the activity enclosed by the ROI projection along the z-axis. Equation (2) holds under the assumption of an infinitesimal thin source located at a well-defined depth d in a homogenous medium with linear attenuation coefficient μ. The ROI activity is thus given by

$$A_{ROI} = \varepsilon_{\text{air}}^{-1} \cdot R \cdot e^{\mu d} \ , \qquad (3)$$

where $e^{\mu d}$ is the attenuation correction factor. In practice, application of equation (3) requires that the count rate R is calculated from a scatter-free projection $p(x,y)$, i.e., that the contribution from all type-4 events have been eliminated from the image. Considerable efforts have been made in the development of scatter correction techniques of 2D projections, primarily considered a pre-processing step for SPECT reconstruction. One technique that has gain widespread use are the dual and triple energy window (DEW/TEW) methods [28-30], in which the scatter contribution in

the primary energy window is estimated pixel-by-pixel from images acquired for one (DEW) or two (TEW) narrow energy windows, adjacent to the primary window. Another common method relies on implicit scatter-correction by an effective attenuation factor $\mu_{eff} < \mu$ in equation (3) [31, 32]. Other methods include scatter build-up factors [33, 34] and scatter response-function modelling [35, 36].

The major drawback with activity quantification from a single projection is that the depth d, and thereby the attenuation correction factor, is difficult to estimate. Therefore, activity quantification in planar imaging is commonly performed by means of the conjugate-view technique [31]. The method requires acquisition of two gamma-camera images or detector measurements with opposing views, typically an anterior projection p_a and one posterior projection p_p with associated count rates R_a and R_p following equation (2), so that

$$\begin{cases} R_a = \varepsilon_{\text{air}} \cdot A_{ROI} \cdot e^{-\mu d_a} \\ R_p = \varepsilon_{air} \cdot A_{ROI} \cdot e^{-\mu d_p} \end{cases}, \tag{4}$$

where d_a and d_p are the depths of the source in relation to the anterior and posterior skin surface, respectively. The geometric mean of R_a and R_p is thus given by

$$\sqrt{R_a R_p} = \varepsilon_{air} \cdot A_{ROI} \cdot e^{-\frac{\mu}{2}(d_a + d_p)} = \varepsilon_{air} \cdot A_{ROI} \cdot e^{-\frac{\mu T}{2}}, \tag{5}$$

where $T = d_a + d_p$ is the total thickness of the patient at the position of the ROI. Thus, the ROI activity is given by

$$A_{ROI} = \varepsilon_{\text{air}}^{-1} \cdot \sqrt{R_a R_p} \cdot e^{\frac{\mu T}{2}}, \tag{6}$$

where the attenuation correction factor $e^{\frac{\mu T}{2}}$ depends only on the patient thickness, and not the source depth. One problem with the conjugate-view method as formulated in equation (5) is that the assumption of a well-defined patient thickness, and resulting attenuation-correction factor, does not generally hold for large organs where the patient thickness may vary considerably across the ROI. This effect can be mitigated by using the conjugate-view method pixel-by-pixel, in which a geometric mean image $p_{GM}(x, y)$ is calculated according to

$$p_{GM}(x, y) = \sqrt{p_a(x, y) \cdot p_p(x, y)}. \tag{7}$$

Using equation (1) for $p_a(x,y)$ and $p_p(x,y)$ and again assuming scatter-free projections and an infinitesimally-thin source for every (x,y)-coordinate, the ROI activity is given by (see appendix 1):

$$A_{ROI} = \varepsilon_{air}^{-1} \iint_{\mathrm{ROI}} p_{\mathrm{GM}}(x,y) \exp\left(\frac{1}{2} \int_{z_{\min}(x,y)}^{z_{\max}(x,y)} \mu(x,y,z)\mathrm{d}z\right) dxdy\,. \qquad (8)$$

The exponential term in equation (8) represents a 2D attenuation map, i.e., the integral of the attenuation coefficient over the patient thickness at position (x,y) along the projection direction. In practice, this map can be obtained by transmission imaging using a ^{57}Co flood source or a CT localiser X-ray image (e.g., "scout", "surview", or "topogram", depending on the manufacturer) [36-38]. As opposed to quantification using equation (6), equation (8) does not presuppose a constant thickness and attenuation for all points in the ROI. Often, an additional correction factor is applied to the ROI activity to compensate for the extension of the source in the z-direction [31].

Although planar image quantification allows for reasonably accurate estimates of the ROI activity, its accuracy in terms of organ activity quantification is ultimately limited by the superposition of different sources of activity in the projection direction. In general, this means that the ROI activity is not equal to the organ activity, and that overlap correction is required. The most common technique is to define an additional ROI in the vicinity of the organ, in order to estimate and subtract the background contribution to the count rate or activity in the organ ROI.

SPECT reconstruction and quantification

In SPECT imaging, a large set of projection images acquired from different angles are used to reconstruct a 3D activity distribution map that is consistent with the measured projections. The dominating reconstruction technique in the early days of SPECT was filtered back-projection (FBP); essentially one of several analytical reconstruction methods used for inversion of the Radon transform [39]. The Radon transform describes the projections at different angles as line integrals of the source distribution. As such, it represents imaging with perfect collimation and without photon attenuation and scattering in the object. The inverse Radon transform, i.e., FBP reconstruction, is thus incapable of compensating for these effects. Therefore, quantitative SPECT with FBP requires either pre-processed projection data or post-processing of the reconstructed slices to be quantitatively accurate. Furthermore, FBP SPECT images are hampered by streak artefacts and noise enhancement due to limited angular sampling and absence of noise modelling. Although more complex

versions of the Radon transform can be formulated, general analytical solutions are difficult to find [39]. For these reasons, FBP has largely been replaced in clinical practice by iterative reconstruction methods. These methods are generally more computationally demanding, but also more suitable for incorporation of complex models of the underlying imaging physics and the statistical variability (noise) in the acquired projections.

Iterative reconstruction techniques are particular variants of optimisation algorithms that aim to find the best estimate of the 3D activity distribution, given the measured projections and a goodness-of-fit criterion. In iterative reconstruction, the activity distribution is considered to be discrete, i.e., $f(x,y,z) = f_j$ with j denoting the voxel index. The acquisition of projection images is described by

$$p_i = \sum_j a_{ij} f_j \,, \tag{9}$$

where p_i denotes the number of detected counts in pixel i, and a_{ij} is the expected contribution from photons originating from voxel j to the counts detected in bin i. Equation (9) may also be written in matrix form according to $\boldsymbol{p} = \boldsymbol{A}\boldsymbol{f}$, where $\boldsymbol{A}$ is the so called system matrix with elements a_{ij}. The system matrix can be considered as the model of the imaging process, and should ideally contain all the important image-deteriorating effects, including object-dependent photon attenuation and scattering, as well as the limited spatial resolution due to the collimator-detector response function [40].

The most widely-used iterative reconstruction method in SPECT is the maximum-likelihood expectation maximisation (ML-EM) algorithm [41]. The algorithm aims to find the statistically best estimate of the activity distribution by maximising the log-likelihood function $l(\boldsymbol{f}) = \ln(\Pr(\boldsymbol{p}|\boldsymbol{f}))$, where $\Pr(\boldsymbol{p}|\boldsymbol{f})$ is the conditional probability of obtaining the projection data $\boldsymbol{p}$ given the activity distribution $\boldsymbol{f}$. In SPECT imaging, the probability of detecting exactly p_i counts in projection bin i is given by a Poisson distribution with expectation value λ_i:

$$\Pr(p_i|\lambda_i) = \frac{\lambda_i^{p_i} e^{-\lambda_i}}{p_i!}. \tag{10}$$

Assuming that the number of counts detected in each pixel are independent, and that the system matrix $\boldsymbol{A}$ is a correct model of the imaging process so that $\lambda_i = \sum_j a_{ij} f_j$, the appropriate log-likelihood function is given by

$$l(\boldsymbol{f}) = \sum_i \left(p_i \ln\left(\sum_j a_{ij} f_j \right) - \sum_j a_{ij} f_j - \ln(p_i!) \right). \quad (11)$$

The ML-EM algorithm maximises the log-likelihood by an iterative scheme with guaranteed convergence to the best possible estimate in terms of maximum log-likelihood. The algorithm is described by [42]:

$$f_j^{n+1} = \frac{f_j^n}{\sum_i a_{ij}} \sum_i a_{ij} \left(\frac{p_i}{\sum_k a_{ik} f_k^n} \right), \quad (12)$$

where f_j^n is the estimate of the value in voxel j after n iterations, and p_i is the measured projection data. The algorithm requires an initial estimate of the 3D source distribution $f_j^0 > 0$. The expected projection data that would arise from this distribution are calculated according to equation (9), and compared to the measured projection data by division. The resulting ratio of measured to estimated projection data is then backprojected into the 3D domain, and the current estimate is subsequently updated by multiplication with the normalised backprojection, which completes the first iteration. The new estimate is used as starting point for the next iteration, and the entire process is repeated until convergence is reached.

The implementation of ML-EM in SPECT reconstruction is normally not performed by explicit use of the system matrix $\boldsymbol{A}$, due to the impractically-large number of elements required for most clinical applications. Instead, the reconstruction algorithm relies on a projector-backprojector model for calculating the projections and backprojections "on the fly" without storing the matrix elements between subsequent iterations [43, 44]. Compensation for attenuation, scatter, and distance-dependent resolution can be performed by including these effects in the projector-backprojector model. For instance, the attenuation of photons originating from a specific voxel to a specific projection bin can be calculated using a patient-specific map of attenuation coefficients, which in turn can be derived from a CT study. The increasing availability of hybrid SPECT/CT systems has made attenuation correction increasingly available in clinical practice. Scatter correction in SPECT can be performed either by pre-reconstruction correction of the planar projections as previously discussed, or by including the scatter contribution in the projector model. The scatter contribution in the forward projections can be estimated with a variety of methods, such as by DEW/TEW measurement, analytical calculation [45], by convolution with pre-calculated or model scatter kernels [46, 47], or utilising full Monte Carlo simulations [48].

The main drawback with ML-EM reconstruction is the suboptimal convergence properties. The convergence rate is slow and object-dependent; it is

not the same across all positions in a heterogeneous image. A relatively large number of iterations (~20-100) is therefore often required to obtain an accurate activity-distribution estimate, and the required computation time puts a limit to its practical applicability. To meet this shortcoming, accelerated versions of the ML-EM algorithm have been developed. The most widely used is the ordered-subset EM (OS-EM) algorithm, in which only a subset of the projection data is used to update the current estimate [49]. OS-EM suffers from some theoretical concerns, but provided that the subset size and ordering is chosen with some caution, the OS-EM reconstructions closely approximates the ML-EM reconstructions in most relevant scenarios [40].

The SPECT image $\hat{f}(x,y,z)$ represents an estimate of the photon emission density in 3D (emissions/unit volume). The activity in a VOI is thus obtained according to

$$A_{VOI} = (\varepsilon_0 t)^{-1} \iiint_{VOI} \hat{f}(x,y,z)dxdydz \ , \tag{13}$$

where t denotes the total acquisition time of the acquired projections. Image segmentation is generally more tedious and time-consuming in SPECT than in planar imaging because it may involve delineation of the structure in a large number of SPECT slices. The segmentation process may be facilitated by a co-registered CT image providing anatomical information.

One major factor that impairs the accuracy of quantitative SPECT is the partial volume effect (PVE), resulting from the limited spatial resolution of the gamma camera [50]. The PVE leads to a blurring of the image and 'spill-over' of counts between adjacent voxels. If compensation methods are not applied, the spill-over leads to an underestimation in objects that have a high activity concentration compared to their surroundings, and conversely to an overestimation in objects with low activity concentration compared to their surroundings. Compensation for PVE may be performed as a part of iterative reconstructions algorithm by incorporating spatial resolution modelling in the projector-backprojector models [51, 52]. This approach has been shown to reduce, but not eliminate, the impact of the PVE in quantitative SPECT, but also to produce Gibbs-like ringing artifacts [50, 53]. Depending on the size of the object and the ROI definition, the ringing artifacts can have a large impact on quantitative estimates. Other compensation methods rely on post-processing using estimated recovery coefficients measured in standard phantom geometries [54], or by modelling the resolution effects on binary ROI templates [53].

4. Monte Carlo methods in nuclear medicine

The Monte Carlo method is a useful calculation tool with many applications in nuclear medicine, ranging from detector development and characterisation, to imaging simulations, image reconstruction, and internal dosimetry [55]. The method is based on sampling of a large number of outcomes from statistical probability density functions (PDFs) using (pseudo-)random number generators, and is often successful in solving problems where analytical approaches fail. The name was established at Los Alamos National Laboratory during the Manhattan project, and stems from the city of Monte Carlo with its world renowned casinos, due to the conceptual similarities between random sampling and throwing a dice.

The Monte Carlo method is in theory exact in the limit of an infinite number of histories, but the reliability of any results obtained are ultimately determined by the models used to describe the studied system. Furthermore, the computation time required to simulate a sufficient number of histories may, for some problems, be too large for practical implementation. Thus, even if the system can be perfectly described, approximations and simplified models are often required to achieve realistic computation times. Finally, it is essential that the random number sequence used for sampling is truly random, or that it closely approximates the properties of a random sequence. In practice, computer algorithms are often used to calculate pseudo-random numbers, starting from an initial seed value.

In nuclear medicine, the main use of the Monte Carlo method is to model the production, transport, and energy deposition pattern of ionising radiation in different media. The Monte Carlo approach is suitable for this problem because the relevant physical processes can be described by PDFs, often in the form of differential cross-sections. Monte Carlo simulations are often performed for internal dosimetry applications, and for research on radiation detection and imaging systems. A large number of Monte Carlo programs have been developed and made publically available. In essence, they can be categorised as general-purpose programs or photon-tracking programs. The general-purpose programs are capable of simulating coupled photon and particle transport, which is required for dosimetry research. Examples of such programs are PENELOPE [56], GATE/GEANT4 [57], and various versions of the MCNP[58] and EGS code packages [59]. The photon-tracking programs, such as SIMIND [60] and SimSET [47], are less flexible in terms

of possible applications, but also less complex and in many aspects also more user-friendly. Due to the absence of particle tracking, their usefulness for radiation dosimetry is limited. Conversely, they are optimal for nuclear medicine imaging research owing to their computationally-efficient simulations of SPECT, PET, and planar gamma-camera imaging.

Two different Monte Carlo programs have been used in this work; SIMIND and EGS4. SIMIND has been developed and optimised specifically for simulating gamma-camera imaging, while EGS4 is a general-purpose program useful for internal dosimetry. A brief description of these programs is given below.

The SIMIND Monte Carlo code

The SIMIND Monte Carlo program was first described in a peer-reviewed article in 1989 [61], and has been in active development since. A more recent description of the program and its features is given in [60]. SIMIND is a photon-tracking program that simulates gamma-camera imaging in planar or SPECT mode. In short, a text-based configuration program is used to define the source and density distribution, the properties of the gamma camera, and which results to extract from the simulations. SIMIND supports imaging simulations based on heterogeneous voxel phantoms as well as homogenous standard shapes such as cylinders, spheres, and cuboids. Because the history of each photon is exactly known, it is possible to study parameters that are impossible to obtain by measurement. In addition, it is possible to study the quantitative accuracy of measurements based on image data, because all parameters relating to the activity distribution in the object are known. The camera model in SIMIND consists of a scintillation crystal, a collimator, a protective cover, and optionally a uniform backscatter layer to simulate photon interactions in the photomultiplier tubes and electronics in the detector head. The included collimator database contains data for the majority of commercially available systems, which facilitates the set-up for simulation of clinical camera systems.

Several variance reduction techniques have been implemented to increase the computational efficiency, in essence by decreasing the amount of histories required to obtain sufficient statistics. One example is forced interaction of photons impinging on the crystal. This efficiently reduces the computation time spent on tracking photons without contribution to the obtained image or energy spectrum. Several additional variance reduction techniques are implemented, including forced interaction in the phantom, photon history splitting, and emission direction limiting. Recent development of SIMIND that is not directly related to this work, is focused on SPECT reconstruction [62] and simulation of pixelated solid-state detectors [63] owing to the new generation of CZT-based cameras for myocardial SPECT [23, 24].

The EGS4 code

EGS4 is a general-purpose Monte Carlo program able to simulate coupled transport of photons and charged particles. The code was released in 1985 [64] as a low-energy extension of the electron gamma shower (EGS) Monte Carlo program which originally was developed for high-energy physics applications. The EGS4 program was continuously revised and updated until the late 1990's, when development branched into EGSnrc and EGS5 led by two different groups [59]. In general, the simulation of charged particle transport is a challenge owing to the very large number of interactions occurring in the slowing-down process. In order to allow simulations with reasonable computation time, electron transport is often modelled using the so-called condensed history approach, where the cumulative effect of a large number of interactions is treated in a single step. EGS4 employs a mixed scheme where inelastic scatterings are treated individually, and elastic collisions are grouped and sampled from a multi-scattering distribution.

5. Anthropomorphic computer phantoms

Typically, Monte Carlo simulations in nuclear medicine generally require a definition of the geometry and environment in which the emitted photons and particles should be tracked. In many applications, the geometry is defined by a digital phantom, i.e., a mathematical description of a three-dimensional object of interest. Although small-animal phantoms have attracted increasing interest during recent years [65, 66], most efforts in phantom development have been put into the construction of increasingly realistic human models. The advent of anthropomorphic digital phantoms in nuclear medicine began with the development of the "Fisher-Snyder phantom", which was originally developed at Oak Ridge National Laboratory, Tennessee, USA, and later adopted and renamed as the "MIRD-5 phantom" by the MIRD committee in 1969 [67]. The MIRD-5 phantom is shown in the left panel of figure 5. The generation of stylised phantoms, in which the body and internal organs are described by standard geometrical primitives such as spheres and cylinders, were mainly applied to calculate absorbed fractions and S values (see chapter 7) for subsequent use in calculations of absorbed dose and effective dose.

The major limitation of the stylised phantoms is that the human anatomy is not very well described by a set of quadric equations, which puts a severe limit to the reliability of calculated parameters. This drawback was substantially reduced by the introduction of voxel phantoms, which constituted the second generation of anthropomorphic digital phantoms. A voxel phantom is constituted by a segmented 3D volume, typically based on tomographic CT or MRI data, so that each voxel is classified in terms of which anatomical entity it belongs to. One of the most widely used voxel phantoms is the Zubal phantom, which is based on CT data of an adult male, and consists of 36 segmented anatomical structures [68]. The Zubal phantom, shown in the middle panel of figure 5, was a major improvement to the stylised phantoms in terms of anatomical realism and gained widespread use in nuclear medicine imaging research. Voxel phantoms have also been widely used for radiation protection dosimetry, especially the Adult Reference Computational Phantoms presented by the International Commission of Radiation Protection (ICRP) in 2009 [69]. The UF (University of Florida) family of voxel phantoms including children of different ages, has also had a large impact [70].

The third generation of digital phantoms arrived in the beginning of the 2000's and are characterised by geometrical modelling by boundary representation (BREP), either in the form of polygonal meshes or NURBS (non-uniform rational b-splines). In brief, a BREP phantom is constructed by fitting smooth surfaces to the segmented volumes of a voxel phantom. The BREP phantoms are superior to the voxel phantoms with regards to flexibility. Voxel phantoms are constrained to a specific geometry; however, the BREP phantoms can easily be modified by standard tools and software developed for computer graphics and computer-aided design. In addition, the BREP technique facilitates realistic surface deformations that are useful when changing the volume and positions of different organs, simulating breathing and cardiac motion, or changing the posture of the phantom. The perhaps most prominent BREP phantoms for nuclear medicine are the NCAT/XCAT phantom series [71]. The NCAT phantom was the first described NURBS-based anthropomorphic designed for nuclear medicine imaging research, and consisted of a torso model with possibility of simulating cardiac and respiratory motion. The NCAT phantom was eventually succeeded by the whole-body XCAT phantom [72], which was created by digital segmentation of the Visible Human anatomical image dataset [73]. Due to the high level of detail and spatial resolution of the data on which it is based, the XCAT phantom is more anatomically realistic than its predecessor and is today considered a state-of-the-art digital phantom for nuclear medicine imaging research. XCAT is distributed as a NURBS template file, a computer program, and a user-adjustable input file. The program processes the NURBS surfaces according to the user input, and outputs a corresponding voxel phantom with arbitrary voxel size. Originally, the phantom was available in one male and one female version that could be modified by scaling length, width, and organ volumes to generate phantoms with some degree of anatomic variability. Although this approach can be used to generate phantoms of different sizes, it was not considered sufficiently flexible to capture the full internal anatomical variation of a patient population. This limitation was recently addressed in a publication announcing a population of 58 unique phantoms and based on CT data of patients of different length, width, and age [74]. The UF family of computer phantoms have also been re-modelled from its voxel predecessors to BREP versions [75, 76] and have quite recently been extended with the addition of pregnant females at eight different fetal ages [77].

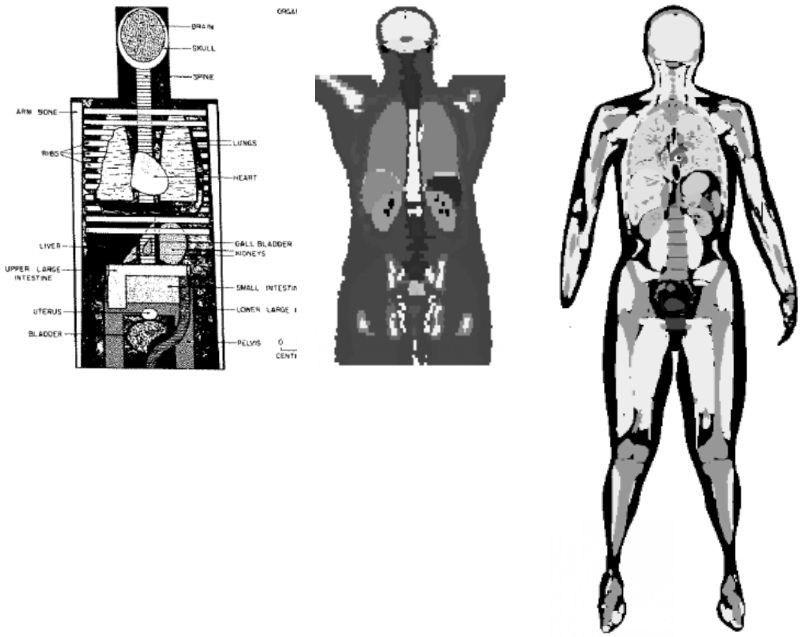

Figure 5. Three generations of computational phantoms developed for dosimetry and imaging research in nuclear medicine. Left: Schematic illustration of the Mird-5 Phantom (1969) [67], reprinted with permission (This research was originally published in *JNM*. © by the Society of Nuclear Medicine and Molecular Imaging, Inc.[1]). Centre: Central coronal slice of the Zubal voxel phantom (1994) [68]. Right: Central coronal slice of the original female XCAT phantom (2010). [72] The Zubal and XCAT phantoms should not be compared by greyscale because the voxel values simply represent integer code numbers identifying all voxels belonging to a certain anatomical structure.

[1]Snyder et al. MIRD Pamphlet #5 Revised: Estimates of absorbed fractions for monoenergetic photon sources uniformly distributed in various organs of a heterogeneous phantom. 1975

6. Pharmacokinetics and compartment models

Pharmacokinetics is a general term used to describe the time-course of a substance with regards to distribution, retention, metabolism, and clearance of the substance in and from the body after administration. In RNT, pharmacokinetic (PK) models can be utilised for pre-therapy dose planning and potentially also for improved TAC estimation in patient- and organ-specific absorbed dose calculations [78]. Pharmacokinetic models are also used in the diagnostic setting. A few notable examples includes determination of the glucose metabolic rate using ^{18}F-FDG PET [79], quantifying (effective) renal plasma flow following administration of ^{131}I-OIH [80], and dopamine receptor-ligand binding studies using ^{11}C-raclopride PET [81].

The pharmacokinetic properties of a radiopharmaceutical are often described in the context of a compartment model. The compartments of such a model represent different states in which the radiopharmaceutical or its metabolites may exist, for instance in terms of chemical state or localisation in the body. The parameters of a compartment model are called transfer rate constants and describe the probability for a single unit of tracer to be transferred from one compartment to another, per unit time. Thus, the rate of outflow from a compartment is proportional to its contained amount. A compartment system can be described by a set of linear, first-order differential equations according to:

$$\frac{dA_i(t)}{dt} = \sum_{j=1}^{n} k_{ji}A_j(t) - k_{ij}A_i(t)\,, \qquad (14)$$

where n is the number of compartments, $A_i(t)$ is the amount contained in compartment i at time t, and k_{ij} is the rate constant for transfer from compartment i to compartment j in units of reciprocal time (often min^{-1}). If a constant volume V_i is assigned to the compartments, equation (14) can also be reformulated in terms of compartmental concentrations:

$$\frac{dC_i(t)}{dt} = \frac{1}{V_i}\sum_{j=1}^{n} r_{ji}C_j(t) - r_{ij}C_i(t)\,, \tag{15}$$

where r_{ij} is the compartmental clearance, (ml·min^{-1}), which may be interpreted as an effective flow of the solvent from compartment *i* to compartment *j*, given by

$$r_{ij} = V_i \cdot k_{ij}\,. \tag{16}$$

Strictly, the transfer rate constants in equation (14) and (15) do not necessarily need to be constant with regards to compartment contents or time. In such cases, the compartment model is non-linear or time-dependent. In this work, only linear time-independent models have been considered.

The system of equations describing a compartment model has analytic solutions, but these increase in complexity with the number of compartments. A practical alternative for $n \gtrsim 3$ is to use a numerical method, such as the well-established and robust 4th-order Runge-Kutta algorithm [82], to obtain numerical solutions for $A_i(t)$.

7. Internal dosimetry

Internal dosimetry deals with the assessment of absorbed dose to different organs and tissues due to irradiation from radioactive sources located in the body. The motivation for dosimetry is that organ absorbed doses, or quantities derived from them, are predictive of the risk for cancer induction in an population [83] or of a specific biological effect in an individual [20] after exposure to ionising radiation.

In diagnostic nuclear medicine, the level of activity and associated absorbed doses are too low (~mGy range) to induce deterministic effects, i.e., observable biological effects that can be directly linked to the exposure of the individual. The widely adopted [84] but debated [85] linear-no-threshold (LNT) model states that even very low exposures to ionising radiation increases the risk of stochastic effects, primarily cancer induction, thereby motivating the use of dosimetry in diagnostic nuclear medicine. Although organ absorbed doses can differ substantially from one patient to another, traditionally there has not been a large interest in patient-specific dosimetry, given the small hypothetical risk increase in relation to the associated uncertainty and to the baseline life-time risk of developing cancer. Instead, internal dosimetry is used to calculate organ-absorbed doses to a reference phantom that should be representative for an entire patient population [69]. These doses are subsequently used for calculation of the effective dose [86, 87], which is useful for risk assessment and comparison between different diagnostic modalities or radiopharmaceuticals.

In RNT, the aim is to deliver a high absorbed dose to the target tissue and thereby achieve a biological response and treatment effect. Unfortunately, this often involves irradiation of non-targeted, healthy tissue to an extent where there is a non-negligible risk for radiation-induced adverse effects. The uptake and retention of activity in normal organs generally exhibit a large variability between patients, in turn resulting in a large variability in the absorbed dose. Consequently, dosimetry is required on a patient-specific basis rather than as an average for a population of patients.

The MIRD formalism and image-based dosimetry

The most widely adopted mathematical formulae for internal dosimetry is the so-called MIRD formalism [88]. The MIRD formalism is characterised by factorising the expression for absorbed dose into two factors; one describing the uptake and retention of activity in the source r_S, and one describing the energy absorption in the target r_T from ionising radiation emissions from r_S. In clinical nuclear medicine, r_T and r_S are commonly constituted by different organs, and the mean absorbed dose D to r_T after administration of a radiopharmaceutical at $t = 0$ is calculated according to

$$D_{r_T} = \int_0^\infty R_{r_T}(t)dt = \int_0^\infty \sum_{r_S} A_{r_S}(t) \cdot S(r_T \leftarrow r_S)\, dt = \sum_{r_S} \tilde{A}_{r_S} \cdot S(r_T \leftarrow r_S) \tag{17}$$

where $R_{r_T}(t)$ is the absorbed-dose rate in r_T and $A_{r_S}(t)$ is the activity in r_S, both at time t. $S(r_T \leftarrow r_S)$ is the so-called S value or dose-conversion factor describing the radiation transport from source to target. $\tilde{A}_{r_S}$ is the cumulated activity, i.e., the total number of decays in the source region, given by

$$\tilde{A}_{r_S} = \int_0^\infty A_{r_S}(t)dt\,. \tag{18}$$

Hence, the task of internal absorbed dose assessment can be considered to consist of two separate problems; namely, to determine the different source organ TACs $A(r_S, t)$ and to calculate or apply appropriate pre-calculated S values.

The TACs of the source organs can be determined by quantitative gamma-camera imaging performed on multiple occasions after administration of the radiopharmaceutical, provided that the emission spectrum of the therapy radionuclide includes photon components with appropriate energy and sufficient yield. If no such emissions exist, pre-therapy dose-planning can be performed by administration of a smaller amount of another radiopharmaceutical with the same targeting properties. However, this approach is cumbersome and prone to errors, because the pharmacokinetics may be affected by both the amount of targeting substance and the radionuclide itself, in addition to other factors related to the state and physiology of the patient that may differ between the time of dose-planning and the time of therapy. Another option specific for high-energy beta-emitters, such as

^{90}Y, is to utilize the bremsstrahlung photons generated in the patient as a secondary product [89].

The S value describes the average amount of energy absorbed per unit mass due in r_T to one nuclear transformation in r_S, and is thus dependent on the emission spectrum of the particular radionuclide but more notably also on the patient geometry. The S value can be further factorized according to

$$S(r_T \leftarrow r_S) = \frac{\Delta\phi(r_T \leftarrow r_S)}{m_{r_T}}, \tag{19}$$

where Δ is the mean energy released to photons and electrons per decay, $\phi(r_T \leftarrow r_S)$ is the absorbed fraction of energy in the target region r_T from emissions in r_S, and m_{r_T} is the mass of the target region.

The traditional approach in internal dosimetry is to apply tabulated S values that have been pre-calculated for various radionuclides and reference phantoms. Although this methodology may be sufficient in some applications, it does not consider the geometry of the individual patient which puts a limit to the accuracy of absorbed-dose estimates. The first-order individualization of the dosimetry is to rescale the pre-calculated S values with the mass of the organ in the specific patient. From equation (19), this is equivalent to assuming equal absorbed fractions in the phantom and patient. A further refinement of patient-specific dosimetry is to use 3D SPECT or PET images of the activity distribution in the patient, and calculate the absorbed dose on a voxel-by-voxel basis [90]. Depending on the emission spectrum of the radionuclide in relation to the voxel size, this is performed by either by assuming local (intravoxel) energy deposition, using voxel S values, convolution with point-dose kernels, full Monte Carlo radiation transport calculation, or by a combination of these methods.

8. Dynamic renal scintigraphy

Between five and six thousand dynamic renography studies with ^{99m}Tc-MAG3 are performed in Sweden each year. MAG3 (Mercapto-tri-glycine) was first introduced in 1986 [91] and a kit formulation for simplified synthesis was developed and available for studies shortly thereafter [92]. Owing to its superior properties in terms of imaging characteristics, availability, and price, ^{99m}Tc-MAG3 has almost completely replaced the previously used renal tracers, such as ^{99m}Tc-DTPA (diethylene-triamine-pentaacetic acid), ^{131}I-OIH (ortho-iodo-hippuran), and ^{123}I-OIH.

Following the study procedure as outlined in the introduction of this thesis, analysis of the obtained data is performed by visual review of the image sequence, accompanied by quantitative or semi-quantitative region-of-interest (ROI) analysis. The background-corrected count rate in each kidney ROI as a function of time is called the renogram (figure 6), and different parameters of this curve are often quoted and used as clinical indicators. The relative renal function (RRF), i.e., the contribution of each kidney to the total renal function, is also calculated on the basis of these curves. This can be performed with various methods of different levels of sophistication. The most straight-forward approach is the integral method, which simply relies on the integral of the renograms (sum of counts) during a specific time-interval. The time-interval should be selected so that there is minimal contribution from the activity bolus in the renal arteries, and negligible outflow of tracer from the kidneys. In practice, the recommended interval is between 1 min and 2.5 min post-injection [93]. The RRF may also be calculated by the mean slope method [93], or by methods relying on a vascular input function such as the Patlak-Rutland method and deconvolution techniques [94, 95]. The vascular input function may be estimated from the count rate in a cardiac ROI. A recent study suggests a simplified approach for measurement of the RRF without the need for background subtraction [96]. In this method, the renal input function is estimated from a ROI over the liver.

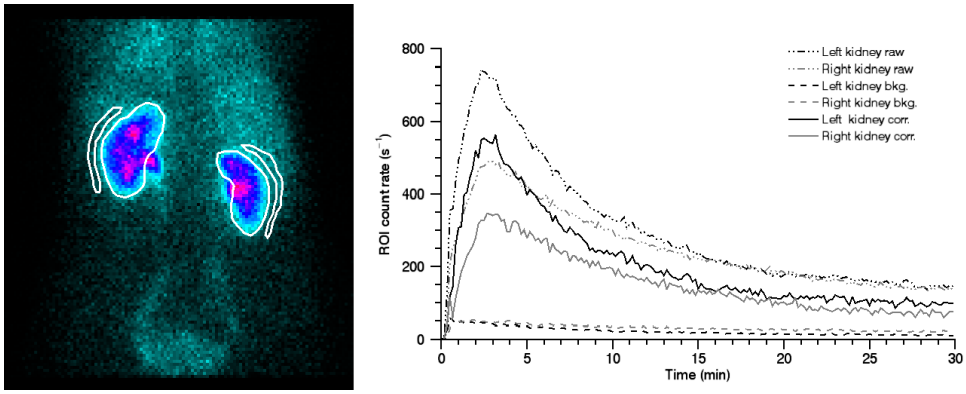

Figure 6. Left: Example delineation of renal and background regions-of-interest in ^{99m}Tc-MAG3 studies. Right: Count rate as a function of time in the different ROIs (dashed and dot-dashed lines), and the resulting renograms, i.e., background-corrected count rate curves in the renal ROIs (solid lines). Renography study downloaded from the *database of dynamic renal scintigraphy* [42].

The renogram is often considered to represent the kidney TAC, i.e., the activity content of the kidney as a function of time. If the camera system has been calibrated, it is possible to obtain quantitative estimates of the renal activity uptake and thereby the plasma clearance of the radiopharmaceutical [97-99]. As previously discussed, this conversion from counts per second to activity is not straightforward. Owing to the limitations of 2D imaging, it is difficult to accurately eliminate the contribution from other tissues that overlap the kidneys in the anterior-posterior direction. Furthermore, the attenuation and scattering of photons in the patient affect the measured count-rate to an extent that is determined by the specific geometry of the patient. The kidney depth, i.e., the distance to the posterior skin surface, in adult patients is normally around 8 cm which can be compared to the half-value depth of around 4.5 cm for 140-keV photons in soft tissue [27]. Hence, attenuation correction is required for quantitation with reasonable accuracy. Current methods rely on image acquisition with a single camera-head posterior to the patient, and activity quantification using equation (3) with an estimated value of the kidney depth and combined correction for attenuation and scatter using an effective attenuation coefficient. The kidney depth is sometimes estimated from lateral projections, and sometimes calculated using regression equations to predict the depth of the kidneys based on the length and weight of the patients [100]. The latter may be accurate on average for a large group of patients, but deviations of several cm between the predicted and actual depth of the kidneys may occur for individual patients. A possible alternative approach would be to adopt techniques for planar activity quantification used in image-based dosimetry [101], i.e., using equation (8) and incorporating explicit scatter correction of the projection data and pixel-based attenuation correction by transmission scanning with a ^{57}Co flood source or an X-ray CT localiser image.

^{99m}Tc-MAG3 Pharmacokinetics

The pharmacokinetics of ^{99m}Tc-MAG3 have, like most other renal tracers, been thoroughly studied and described in the context of compartment models. After intravenous bolus injection, the measured plasma activity concentration decreases approximately bi-exponentially. This is consistent with a two-compartment model, which is commonly employed to calculate MAG3 clearance based on plasma samples after a single injection [92, 97, 102]. A three-compartment model has also been suggested [103] but its usage, as reported in the literature, appears limited. The models, illustrated in figure 7, consist of one central compartment with one or two peripheral compartments, between which tracer molecules may be transferred. Elimination from the system occurs only from the central compartment, represented by the transfer rate constant k_{10}. The central compartment includes the plasma volume and any other volume in instant concentration equilibrium with it. Thus, the tracer concentration in the central compartment after the bolus injection, can be measured by means of plasma sampling. The bolus is modelled by setting $A_1(0) = A_{inj}$, where A_{inj} denotes the injected activity.

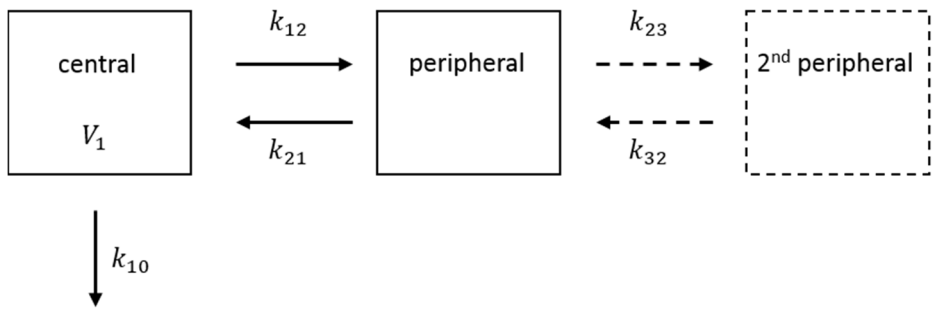

Figure 7. Combined illustration of the two-compartment and three-compartment model for ^{99m}Tc-MAG3 pharmacokinetics. The tracer is administered as a bolus in the central compartment with distribution volume V_1. Transfer between the central and peripheral compartment is represented by transfer rate constants k_{12} and k_{21}. In the three-compartment model, a second peripheral compartment is included with associated transfer rate constants k_{23} and k_{32}. Elimination from the body occurs only from the central compartment with transfer rate constant k_{10}, primarily reflecting the renal clearance.

The plasma clearance, Cl_p, is the effective elimination flow, which from equation (16) is given by:

$$Cl_p = r_{10} = V_1 \cdot k_{10}\,, \tag{20}$$

where V_1 is the volume of the central compartment, sometimes called the initial distribution volume, and k_{10} is the transfer rate constant representing irreversible elimination from the central compartment. The right hand side of equation (20) is

equivalent to the injected amount of tracer divided by the integral of its plasma concentration from zero to infinite time (see appendix 2), which is sometimes used as an alternative 'definition' of plasma clearance. The required parameters can be calculated from a bi-exponential curve fit (assuming a two-compartment model) to the measured plasma concentration as a function of time. Figure 8 shows time-activity concentration curves for ^{99m}Tc-MAG3 in plasma, derived from two- and three-compartment model parameters given in the literature. Corresponding curves for two other renal tracers, ^{99m}Tc-DTPA and ^{131}I-OIH, are included for comparison.

The primary elimination mechanism (represented by k_{10}) of ^{99m}Tc-MAG3 after intravenous administration is renal clearance by tubular extraction. Due to the high fraction of plasma protein binding (~90%), the contribution from glomerular filtration to the total renal clearance is low, in the order of 2 % [102, 104]. The extraction fraction is in the range 0.4 – 0.6 [105]. According to Fick's principle, the renal plasma clearance is equal to the renal blood flow multiplied with the extraction fraction. Assuming a renal plasma flow of 600 ml/min, a typical value of the renal clearance of ^{99m}Tc-MAG3 in normal healthy subjects is around 300 ml/min. Within 30 min after injection, about 75 % of the injected activity has been excreted into urine. A small fraction of ^{99m}Tc-MAG3 is eliminated by hepatobiliary excretion, which may be observed in dynamic renography studies as activity accumulation in the liver and gallbladder. The extra-renal plasma clearance of ^{99m}Tc-MAG3 has been estimated to be 5 % of the total plasma clearance [106]. This result is consistent with activity uptake in the liver, gallbladder, and gastrointestinal tract, measured in patients and normal volunteers [92]. The mean renal parenchymal transit time has been estimated to be approximately 2.5 min in hydrated adults, which is closely related to $T_{\max}$, the time to the peak of the renogram [107]. The latter is a standard renogram parameter which for healthy subjects is approximately between 3 and 4 min [108].

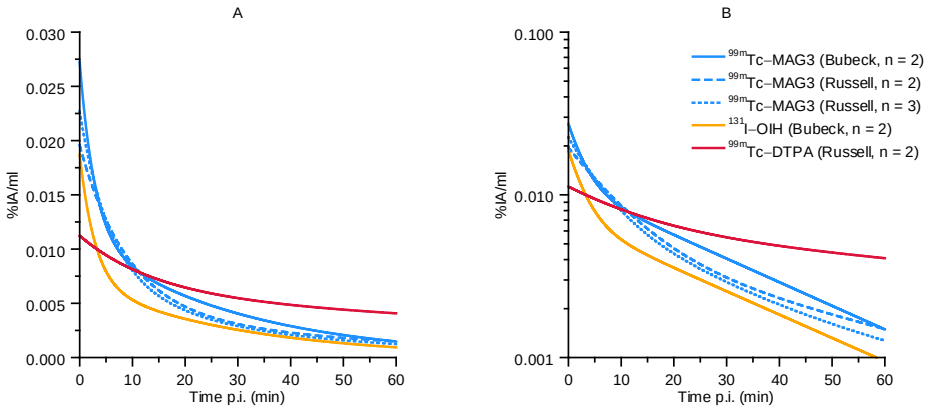

Figure 8. Plasma activity-concentration curves as a function of time according shown on a linear scale (A) and on a logarithmic scale (B). The curves have been reconstructed from compartment model parameters as given by Russell for ^{99m}Tc-MAG3 (n = 2,3) [103] and ^{99m}Tc-DTPA (n = 2) [109], and by Bubeck for ^{99m}Tc-MAG3 and ^{131}I-OIH (n = 2) [102].

Patient models and renography simulations

In paper I, we describe the development of a patient model for simulation renography studies with ^{99m}Tc-MAG3. The patient model was constructed on the basis of the XCAT anthropomorphic digital phantom [72] and the two-compartment PK model for MAG3 described above. The PK model does however only account for the blood clearance of the tracer and not for the typical features that are visualised by renography. The PK model was therefore extended to account for the transport of tracer through the kidneys and accumulation in the urinary tract and urinary bladder, as well as the liver uptake. The tracer transport through the kidneys was modelled by delay lines, consisting of several serially-linked compartments, to enable shaping of the transit time distribution for the renal cortex, medulla, and pelvis separately. Baseline values of the model parameters, i.e., transfer rate constants and transit times, were established mainly based on pharmacokinetic data from literature [102, 106, 107] and to a small extent by comparing simulations to patient images. The compartmental time-activity curves were then used to calculate time-activity curves for all anatomical structures in the XCAT phantom.

A computer program was written in IDL (Exelis Visual Information Solutions, Boulder, CO), for interactive development of the PK model, adjustment of model parameters, implementation of the RK4 solver [82], and display of the phantom activity distribution as shown in figure 9.

Using the voxel phantoms and the calculated TACs, simulations of dynamic studies were implemented in the Monte Carlo program SIMIND. Figure 10 shows example data obtained from simulations of a phantom with varying left-to-right kidney uptake rate corresponding to a RRF of 10/90 (% sin/dx), 30/70, 50/50, 70/30, and 90/10. The variation was achieved by adjusting the ratio of the two transfer rate constants representing the left and right kidney uptake rate, while keeping their sum constant.

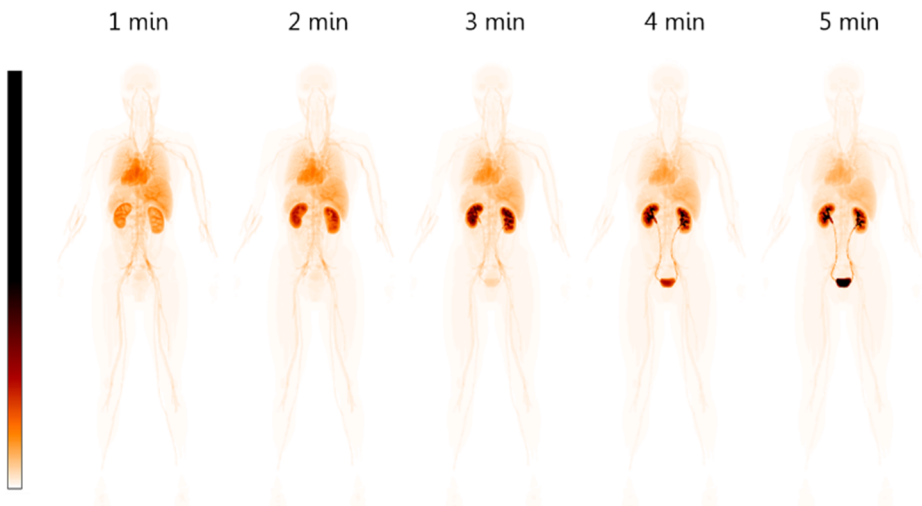

Figure 9. 2D total-activity projection images of the patient model, i.e., the phantom 3D activity distribution, at 1, 2, 3, 4, and 5 min post-injection. The sum of activity is constant in time (physical decay excluded).

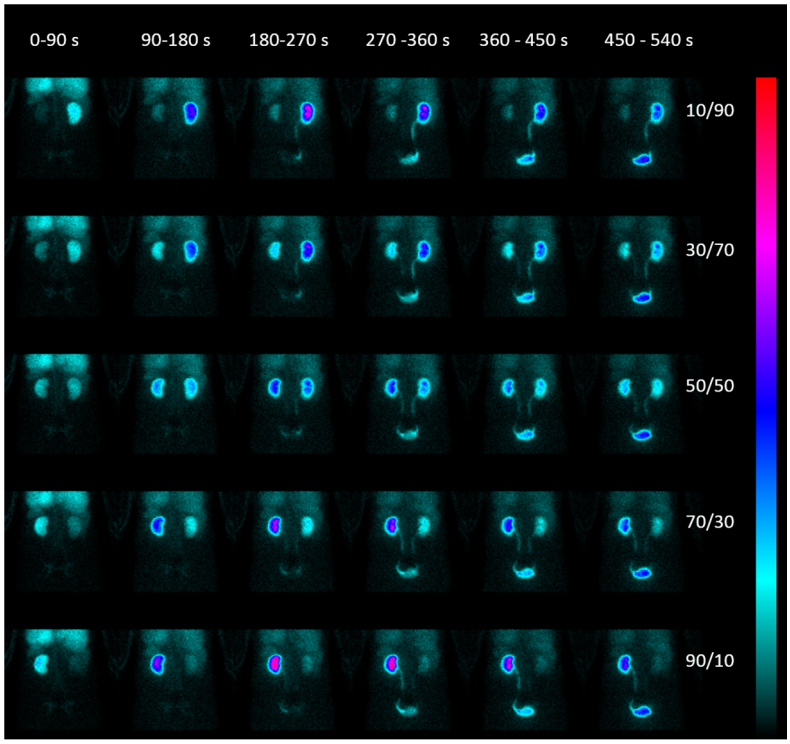

Figure 10. Example simulations of ^{99m}Tc-MAG3 studies corresponding to identical subjects with different differential renal function ranging from 10/90 (% sin/dx) to 90/10. The datasets have been condensed to 90-s frames and cropped at 540 s post-injection for display purposes. All images are shown on the same colour scale.

Accuracy and inter-departmental variability of semi-quantitative metrics

In paper II, we used simulated renography studies for a national audit performed in collaboration with Equalis AB, a not-for-profit company providing external quality assessment of laboratory investigations, including nuclear medicine [110]. The aim was to investigate the measurement accuracy and inter-departmental variability of two common parameters in ^{99m}Tc-MAG3 dynamic renography, namely the differential renal function (RRF) and time to maximum renal activity (T_{max}). Three phantoms with varying pharmacokinetic properties, in terms of renal uptake rate, the relative uptake of each kidney (corresponding to the RRF), and the time to maximum renal activity (corresponding to T_{max}), were generated. Using the batch-mode functionality of SIMIND, we performed clinic-specific simulations that matched the gamma camera, the acquisition protocol, and the standard amount of

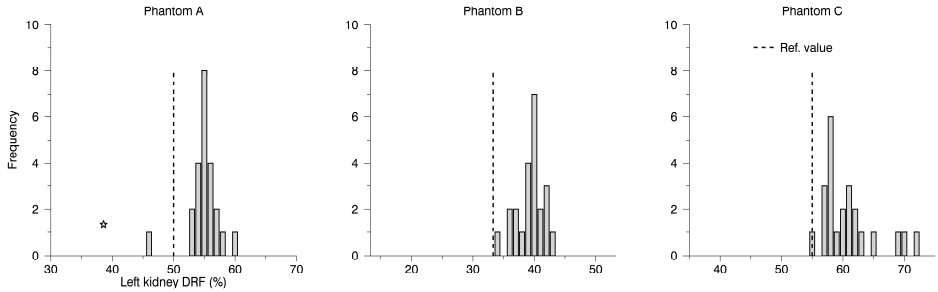

Figure 11. Histograms of relative renal function (RRF) estimates for the left kidney for the three simulated phantoms. The variability for phantom C, simulating a patient with impaired renal function, is higher (range 55-72%) than for phantom A (53-60%) and B (34-43%), owing to a lower kidney-to-background signal ratio. The distributions are biased relative to the reference values owing to photon attenuation differences between the left and right kidney. Figure adapted from paper II.

^{99m}Tc normally administrated at each department participating in the study. The simulated studies were distributed by means of DICOM files that were made available for download. Evaluation of the simulated studies was performed locally using the software and procedures normally used by the participants in clinical routine. Parameter estimates were reported from 21 of the 28 departments performing MAG3 scans as of 2012. The results, illustrated in figure 11, showed that the precision of RRF estimates are dependent on the renal function; the range of RRF estimates were within 7 percentage points (pp) for the phantom corresponding to normal renal function (apart from one outlier excluded from the analysis), but within 17 pp for the phantom corresponding to a patient with severely impaired renal function. The most plausible explanation for this result is the decreased kidney-to-background signal ratio with decreased renal function, which in turn increases the impact of ROI delineation and background subtraction.

The distributions of RRF estimates for the left kidney are shifted approximately 5 pp relative to the reference values, due to a 12-mm depth difference between the left and right kidney in the anatomical phantom used for simulation. These results highlight the importance of the implicit assumption of equal renal depths for RRF calculations based solely on posterior projections, and motivates an investigation of possible improvements of RRF measurements by implementing the conjugate-view methodology. Obviously, the additional value of utilising two opposing projections will depend on the renal depth difference that may be present in patients, in relation to the accuracy that is required from the clinical point of view. Considering the lack of consensus in this issue, further studies are warranted.

9. Dosimetry in PRRT with ^{177}Lu-DOTATATE

As discussed in the introduction, dosimetry for ^{177}Lu PRRT can be used to individually-tailor treatment to maximise the treatment activity while maintaining the risk of adverse effects, i.e., renal toxicity, below a pre-defined tolerance level. The appropriate dose limit in PRRT is a subject of debate, owing to legitimate concerns about the translatability of dose limits derived from external beam radiotherapy. One of the current recommendations for PRRT is that the biologically effective dose (BED) to the kidneys should not exceed 28 Gy for patients with pre-existing risk factors associated with loss of renal function, and 40 Gy for patients without such factors [16]. These limits have, slightly adjusted, been adopted in a phase-II clinical trial that is currently undertaken at Skåne University Hospital in collaboration with Sahlgrenska University Hospital (Iluminet, EudraCT, no. 2011-000240-16). The patients included in this trial are treated with repeated administrations of ^{177}Lu-DOTATATE, and the absorbed dose and BED are calculated based on a combination of quantitative SPECT and planar camera images acquired on four occasions within the first week after each administration. Similar dosimetry protocols based on SPECT/CT have been presented by others, e.g., [111, 112], and current recommendations on quantitative SPECT for ^{177}Lu dosimetry are given in [113].

^{177}Lu-DOTATATE pharmacokinetics

^{177}Lu-DOTATATE has a fast turnover compared to other radiopharmaceuticals traditionally used in RNT, such as radiolabelled antibodies used in radio-immunotherapy. After intravenous infusion of ^{177}Lu-DOTATATE the plasma activity decreases rapidly, primarily owing to glomerular filtration and subsequent urinary excretion, but also by diffusion into the extravascular space and subsequent specific and non-specific uptake in tumours and other tissues. Within 30 to 60 min after administration, more than 15 % of the injected activity has been excreted into the urinary bladder, as shown in paper III. At 24 h post-infusion, the plasma activity in patients is typically 1 % or less, whereas the cumulative elimination with urine

reaches approximately 60 % [114, 115]. However, the amount that is ultimately eliminated with urine is highly dependent on the total tumour burden and associated uptake, because this process competes with renal elimination. Besides tumour uptake, most of the injected activity that has not been eliminated within the first 24 h is taken up in the liver, spleen, and kidneys, as visualised in figure 12. A relatively low and uniform uptake in the remainder of the body can also be noted. The low activity in the brain indicates an intact blood-brain barrier that restricts the infiltration of ^{177}Lu-DOTATATE.

As discussed previously, the kidneys are the critical organ in ^{177}Lu-DOTATATE therapy. Therefore, large efforts have been made to identify uptake mechanism and to develop substances that can be used for renal protection. The long-term retention of activity in the kidneys is the result of reabsorption of a small fraction of the radiolabelled peptides from the primary urine after glomerular filtration [116]. The dominating site of reabsorption, and thereby the renal uptake, is the proximal tubules distributed throughout the renal cortex and outer medulla. The reabsorption, and thereby the long-term activity retention and resulting irradiation, is substantially reduced (~15 - 50 %) by co-infusion of positively-charged basic amino acids [117], which has become part of the routine administration protocol.

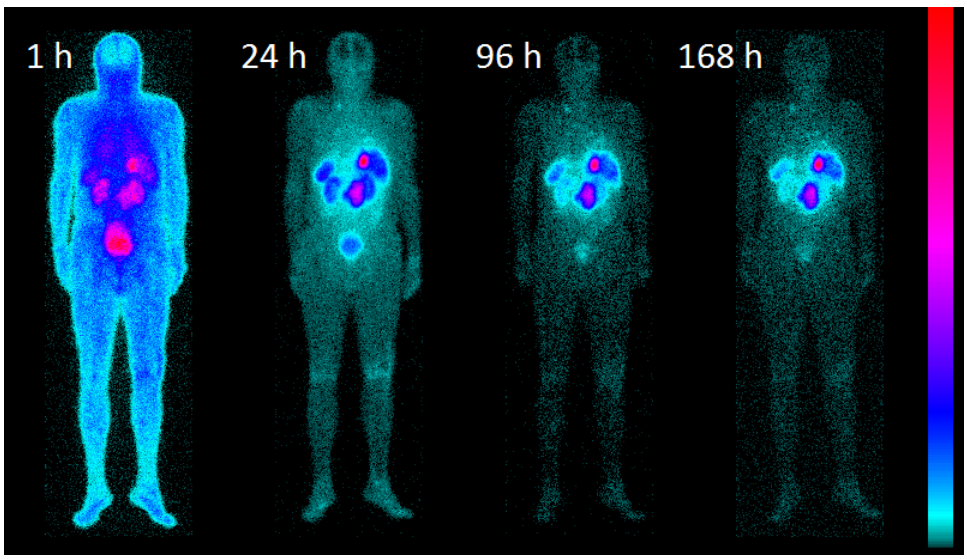

Figure 12. Posterior whole-body scans of a patient on four occasions within the first week after administration of 7400 MBq ^{177}Lu-DOTATATE. At 1 h post-injection (p.i.), a large fraction (~15 %) has already been filtered in the kidneys and excreted into the urinary bladder. The remaining fraction of activity accumulates primarily in the tumours, spleen, liver, and kidneys. Images acquired for dosimetry purposes as a part of the Iluminet clinical trial.

In paper III, we reported measurements of total-body activity and activity concentrations in tumours and the major uptake organs in a group of 10 patients, using a combination of SPECT and planar gamma-camera images. The results, summarized in figure 13, confirmed a high variability in the total-body activity due to a high variability in the tumour burden of the patients. The activity concentrations in the kidneys, liver, and spleen were however relatively consistent between patients. The relative standard deviation for the kidneys was between 20 % and 40 % for the four nominal time points of measurement. The activity concentration in the spleen was slightly higher than in the kidneys at 24 h p.i. and onward. The liver activity concentration was lower, but exhibited slower elimination. Activity concentration measured in tumours were highly variable, mainly due to biological variability, but probably also reflecting the difficulties of accurate activity quantification for small objects due to the PVE, as discussed previously.

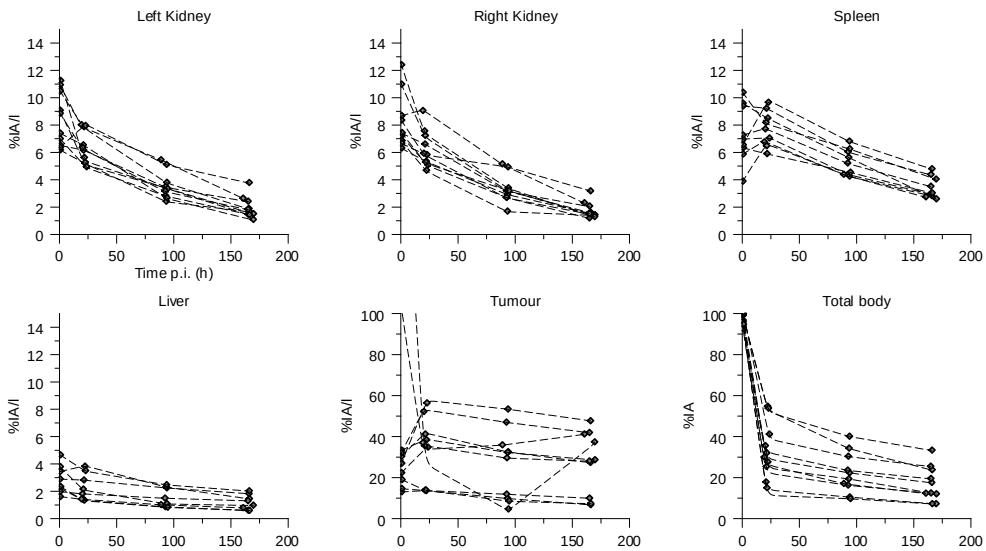

Figure 13. Total-body activity and activity concentration as a function of time in the kidneys, spleen, liver, and tumours, measured in 10 patients after administration of ^{177}Lu-DOTATATE. The dashed lines are included to indicate the set of data points belonging to an individual patient, and do not represent a model fit.

Patient models and reference dosimetry

In paper III, we presented patient models for ^{177}Lu PRRT dosimetry research. Following the methodology in paper I, the patient models were created by coupling a PK model to the XCAT phantom. Three voxel phantoms, representing one male and two females, were generated from the XCAT population. Voxel volumes representing tumours, obtained by segmentation of patient SPECT images, were inserted in the liver and abdomen of the phantoms. A compartment model describing the pharmacokinetics of ^{177}Lu-DOTATATE was constructed with the purpose of calculating and assigning realistic TACs to all phantom organs. The compartment model was restricted to model the uptake in the kidneys, liver, spleen, and tumours, whereas all other organs were merged into a remainder-of-body compartment.

The transfer rate constants of the compartment model were obtained by a fit to patient data, consisting primarily of whole-body activity and activity concentrations in the kidneys, liver, spleen, and tumours measured in a group of ten patients treated with ^{177}Lu-DOTATATE. Activity concentration curves were calculated from SPECT images acquired at 24 h p.i., combined with time-activity curves from planar image data at 1 h, 24 h, 96 h, and 168 h p.i.

Using a similar approach to that described in paper I, the TACs were calculated for all phantom organs by assigning anatomical distribution volumes to all compartments in the kinetic model.

One important aspect in the development of patient models for image-based dosimetry research was to establish reference values of absorbed dose and BED to the organs and tumours. The reference values are useful for evaluation of measurement accuracy, as they represent a ground truth against which calculated estimates can be compared. To this end, we calculated S values for ^{177}Lu in all source-target combinations by transport simulations based on the EGS4 code, described previously. The S values were subsequently used in combination with the phantom organ TACs, $A_{r_S}(t)$, to calculate reference absorbed dose-rate curves $R_{r_T}(t)$, and absorbed dose D_{r_T}, following equation (17).

EGS4 was invoked by the program DOSIMG, an EGS4 wrapper routine previously developed for voxel-based internal dosimetry in nuclear medicine [118, 119]. This program includes features such as calculations of beta spectra, sampling of decay positions, and scoring of energy depositions on a voxel basis. The input to the program is two spatially-aligned 3D maps of equal matrix dimensions representing the activity distribution and the mass density distribution. The radiation emission is sampled from the activity distribution map and the radiation transport is simulated in the mass density map. The result is scored in a new 3D map of equal size, $\boldsymbol{E}_{r_S}$, representing the energy deposition per voxel normalised to a total of 10^6 decays in the source map. To obtain the S values, one simulation was performed for

each source organ r_S in the voxel phantoms. The S values were subsequently calculated according to

$$S(r_T \leftarrow r_S) = \frac{\iiint_{r_T} \boldsymbol{E}_{r_S} dV}{\iiint_{r_T} \boldsymbol{\rho} dV} = \frac{1}{m_{R_T}} \iiint_{r_T} \boldsymbol{E}_{r_S} dV \,, \tag{21}$$

where $dV = dxdydz$ is a volume element, $\boldsymbol{\rho}$ is the 3D mass density distribution map, and m_{R_T} is the mass of the target organ. The DOSIMG/EGS4 program, including the adopted ^{177}Lu radiation emission spectrum, was benchmarked for ^{177}Lu simulations by comparing the absorbed fraction, $\phi(r_S \leftarrow r_S)$ in equation (19), obtained for voxelised spheres of unit density to the corresponding absorbed fractions as given by OLINDA [120]. The relative deviations from OLINDA were less than 1 % for spheres with mass between approximately 4 g and 4 kg (data not shown). The discrepancy was considered acceptable as compared to the uncertainty of image-based absorbed-dose estimates, which is expected to be in the order of 10 % or more.

Uncertainty propagation in image-based patient-specific dosimetry

The uncertainties associated with estimates of the absorbed dose and biologically effective dose (BED) in PRRT, and RNT in general, has long been a subject of debate. In fact, absorbed doses for individual patients reported in the context of PRRT are often presented without estimates of the associated uncertainty [111, 121]. One probable reason for the lack of such estimates is that the complexity of the dosimetry process, with multiple measurement and calculation steps in which the uncertainty propagates, does not readily allow the uncertainty to be expressed by an analytical expression.

The aim of the work presented in paper IV was to thoroughly investigate and calculate the uncertainty of absorbed doses and BED estimates that should be expected in ^{177}Lu-DOTATATE RNT dosimetry when SPECT/CT is used for activity quantification. Although there are many studies related to accuracy and uncertainty in quantitative SPECT, e.g., with focus on VOI delineation [122], effective half-life estimation [123], and gamma-camera calibration [124, 125], there were, to our knowledge, no previous studies where these are propagated to a combined uncertainty in the absorbed dose and BED.

The study was conducted by constructing a computer model of a SPECT/CT-based dosimetry protocol, using the phantoms presented in paper III as patient

models. The modelled dosimetry protocol consisted of SPECT/CT acquisitions on for occasions between zero and seven days post administration. The model components specifically included were:

(i) sensitivity calibration,
(ii) time between activity administration and SPECT acquisition,
(iii) attenuation map estimation from CT,
(iv) SPECT reconstruction with compensation for attenuation, scatter, and distance dependent-resolution,
(v) renal VOI delineation,
(vi) partial volume correction by the use of a recovery factor for the absorbed-dose contribution from electron emissions,
(vii) Monte Carlo simulation of the photon absorbed-dose contribution, and
(viii) curve fitting and integration of the absorbed dose-rate as a function of time.

The uncertainties of the individual components were propagated through the dosimetry process using a Monte Carlo-based framework, to arrive at a statistical distribution of the calculated absorbed dose to the kidneys.

Figure 14 shows the resulting distributions for the kidneys in the three phantoms. The relative standard deviation was approximately 6 % when including all sources of uncertainties. The most important source of uncertainty was shown to be the recovery factor followed by gamma-camera sensitivity calibration. There was a tendency of overestimating the absorbed dose, noted when comparing the distribution means with corresponding reference values. This likely results from mismatch between the shape of the phantom model TAC and the model curve used for fitting in the initial part of the curve (<24 h p.i.), in combination with the temporal sampling schedule. The general shape of the phantom renal TACs for the immediate hours following infusion is supported by dynamic gamma-camera measurements, performed by others [126], during and immediately after infusion. This implies that this results holds merit, and that the renal dosimetry may be improved by excluding the first measurement (~1 h p.i.) in the absorbed dose calculation.

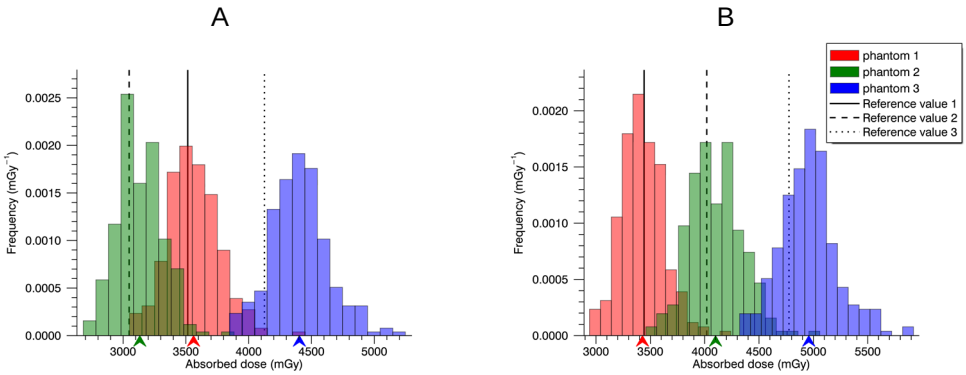

Figure 14. Absorbed-dose histogram for the left kidney (A) and right kidneys (B) in three phantoms. Distribution means are indicated by coloured arrowheads and the corresponding reference values (ideal results) by vertical lines. Figure reproduced from paper IV (http://dx.doi.org/10.1088/0031-9155/60/21/8329) under the terms of the Creative Commons Attribution 3.0 license (https://creativecommons.org/licenses/by/3.0/).

Impact of long-lived radionuclide impurities and imaging schedule

In the production of ^{177}Lu by neutron activation of ^{176}Lu, the isomer ^{177m}Lu is also produced. The fraction of ^{177m}Lu in a stock solution of ^{177}Lu for clinical use is small, and certified by the manufacturer to be less than 0.05 % of the total activity at a reference time after end of production. However, the half-life of ^{177m}Lu (160.4 d) is considerably longer than for ^{177}Lu (6.65 d), meaning that this fraction increases with time. In fact, the presence of ^{177m}Lu has implications in the management of radioactive waste from patient treatment with DOTATATE [127]. In addition, the energy released in form of ionising radiation is on average seven times higher for the metastable isomer. This warrants an investigation on the dosimetric impact of ^{177m}Lu, which is normally not considered in ^{177}Lu PRRT dosimetry. Figure 15 illustrates a simplified decay scheme with the most probable transitions, also showing the origin of the 208 keV photon used for quantitative imaging.

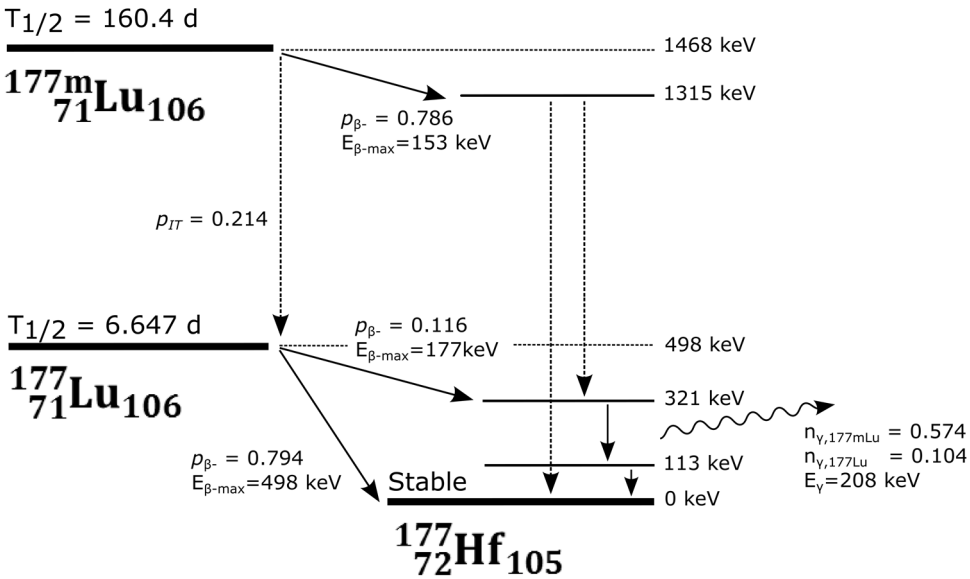

Figure 15. Simplified decay scheme of ^{177m}Lu and ^{177}Lu to ^{177}Hf. Dashed arrows indicate multiple-energy-level transitions. The 208 keV photon is common for both isomers, but emitted with different probabilities (n_γ) with regards to one decay of the parent nucleus. This research was originally published in *JNM*. Sjögreen Gleisner et al. *J Nucl Med*. 2015. **56**, pp. 976 – 984. © by the Society of Nuclear Medicine and Molecular Imaging, Inc.

In paper V, we reported on an investigation of the validity of the standard assumption of negligible contribution from ^{177m}Lu to the absorbed dose following treatment with Lu-DOTATATE. The magnitude of this contribution relates directly to the long-term retention of Lu in the patient after treatment, also emphasising the question of whether the retention is accurately predicted from the standard protocol measurements performed with the gamma camera within the first week after treatment.

Seven patients were, after informed consent, subjected to measurements between 5 and 10 weeks post treatment in addition to the standard protocol measurements. The additional measurements were performed with gamma spectrometers for determination of whole-body activity and planar gamma-camera imaging for assessment of the anatomical activity distribution. Since the 208 keV photon is common to both Lu isomers, their relative contributions to the measurements were calculated starting from a measured value of the radionuclide purity (RNP) at a reference time. RNP was measured in of ^{177m}Lu/^{177}Lu samples using a high-purity germanium (HPGe) detector.

The results obtained in this work showed that the whole-body TAC is slightly underestimated when using measurement data truncated at seven days post-administration, as shown in figure 16. Whole-body absorbed dose increased on average by 5 % (range 2-9 %) for the seven patients investigated when accounting

for ^{177m}Lu and including data from the additional measurements; the main reason being a longer retention of tumour activity than predicted from the routine measurements. The impact of ^{177m}Lu was found to be negligible in the range of RNP values that are guaranteed by the manufacturer, i.e., below 0.05 % at the end of production.

No renal dosimetry was performed in this study, mainly because of poor image quality and counting statistics in the gamma-camera images from five weeks post-administration or later. However, we do not expect that measurements later than one week post-administration will have a large impact on renal absorbed-dose estimates because the long-term retention was mostly confined to tumours. Nevertheless, the results are of importance for the design of protocols for tumour dosimetry or bone marrow dosimetry relying on whole-body activity quantification.

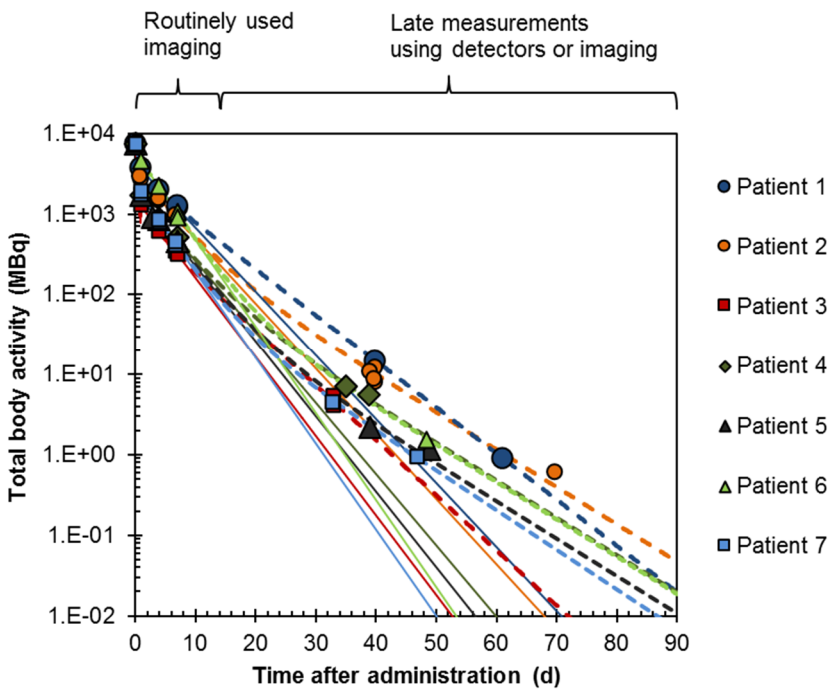

Figure 16. Whole-body time-activity curves for the seven patients investigated. Solid lines are curves fitted to data obtained from routine measurements up to one week post-administration. Dashed lines have been fitted to all data points including the measurements performed between 5 and 10 weeks, resulting in an increased cumulative activity for all patients. Markers and lines representing a single patient are shown in the same colour. This research was originally published in *JNM*. Sjögreen Gleisner et al. *J Nucl Med.* 2015. **56**, pp. 976 – 984. © by the Society of Nuclear Medicine and Molecular Imaging, Inc.

10. Conclusions

Digital phantoms are recognised as a useful and versatile tool for research in medical imaging and dosimetry, and are intimately linked to the Monte Carlo-method for simulations of radiation transport. The development of digital phantoms is ongoing, and much effort is being spent on increasing the anatomical realism, in order to account for anatomical variability, and including physiological aspects such as respiratory and cardiac motion. One of the particularities of nuclear medicine imaging is that many studies are performed dynamically, i.e., to investigate and quantify the activity distribution as a function of time, rather than at a single instant. The main contribution of this work has been the development of pharmacokinetic models that enables simulation of patient-realistic time-dependent activity distributions in digital phantoms, specifically for the radiopharmaceuticals ^{99m}Tc-MAG3 and ^{177}Lu-DOTATATE.

The specific conclusions from the studies in this thesis are summarised as follows:

- Paper I: Patient-like ^{99m}Tc-MAG3 renography studies can be simulated by the Monte Carlo method when coupling a kinetic model to an anatomical digital phantom. Different scenarios of clinical interest can be readily and consistently simulated by varying the parameters in the PK model. The simulated studies are importable to clinical workstations for image analysis following routine clinical procedures.
- Paper II: The results from a national audit revealed a remarkably-high inter-departmental variability in relative renal function estimates for a patient model simulating impaired renal function. This highlighted the need for continuous quality monitoring and arguably also standardisation of processing methods. RRF measurements are biased by renal depth differences due to photon attenuation. For the phantom used, a 1.2 cm difference resulted in a bias of approximately 5 percentage points.
- Paper III: Patient-models were developed and shown to be useful for simulation of realistic SPECT and planar gamma-camera images, and thereby also for research on image-based dosimetry in ^{177}Lu-DOTATATE PRRT. A preliminary evaluation of a plausible dosimetry protocol based on four planar scans and one SPECT/CT indicated that the absorbed dose to tumours and organs can be determined with an accuracy of ± 25 %.

- Paper IV: The uncertainty of renal absorbed dose estimates in ^{177}Lu-PRRT was shown to be approximately 6 % (1 relative standard deviation), by using a computer model of a SPECT/CT-based dosimetry scheme and the phantoms presented in paper III. The largest source of uncertainty was the recovery coefficient that was applied to correct for the partial volume effect, followed by the uncertainty of the gamma-camera sensitivity ($\varepsilon_{\mathrm{air}}$) for ^{177}Lu.
- Paper V: The long-lived metastable isomer $^{177\mathrm{m}}$Lu is measurable in patients several weeks after administration of ^{177}Lu-DOTATATE, but its contribution to the absorbed dose is negligible. The long-term activity retention is underestimated when calculated by extrapolation of measurements performed within the first week post-administration, mostly due to tumour uptake. Measurements performed later than one week post-administration may therefore be warranted, especially if intended for tumour dosimetry.

Outlook

Dynamic renography is a well-established diagnostic method that, despite being challenged by other modalities such as MRI [128], will likely continue its important role in the nearest future, owing to its clinical simplicity and cost-effectiveness. Despite the vast experience with this technique, there is still a need for further improvements. This concerns in particular the large site-to-site variability in RRF estimates shown in paper II. To overcome this issue is obviously not trivial, but efforts such as reference image databases [9] and national audits, presented in this work and by others [129, 130], provide an opportunity for clinics to improve their diagnostic quality. Consensus on image processing methods would probably be helpful to reduce this variability, as would agreement on a minimum set of tools for (semi-)automatic ROI delineation that should be available in renography analysis software.

Dynamic renography as a diagnostic modality could possibly also benefit from full quantification, meaning that the renograms would represent TACs rather than count-rate curves. Although methods for quantitative renography have been developed in the past [97, 98], these do not take advantage of state-of-the-art techniques for patient-specific 2D attenuation and scatter correction used in RNT dosimetry. The phantoms presented in paper I provide realistic reference data sets that are useful for development and evaluation of quantitative methods.

Personalised dosimetry in ^{177}Lu PRRT, and for RNT in general, is undergoing rapid development including initiatives to introduce traceability, uncertainty analysis, and standardised protocols [131]. Currently, dosimetry is mainly performed at specialised research clinics; however, the diversity of methods, lack of

traceability, and unknown uncertainties, mean that there is no guarantee that the absorbed dose calculated at one clinic translates into the same absorbed dose calculated at another. Computational patient models and simulation studies, such as the one performed in this work and in similar efforts by others [132], will likely play an increasingly important role in validation of RNT dosimetry protocols and in facilitating large, multi-centre studies. It should however be acknowledged that not all possible sources of bias and uncertainties can be expected to be captured by this types of simulation studies. For instance, one key parameter with regards to traceability and cross-centre comparison is the calibration of the ionisation chamber that is used to measure the source activity for gamma-camera calibration and for patient treatment. Activity meter specifications, dial settings, calibration procedures, and traceability to primary standards, are seldom or never reported in dosimetry studies, and more efforts are consequently needed in this area.

The dosimetry pipeline developed in paper IV constitutes a useful tool to further optimise ^{177}Lu PRRT dosimetry, considering that it facilitates evaluation of the impact of methodological changes both in terms of accuracy and precision of absorbed-dose calculations. The partial volume effect and use of a fixed recovery factor was found to be the most influential factor on the overall uncertainty, and thus a thorough investigation of patient-specific partial-volume correction is warranted, for example as described in [133].

Acknowledgements

I would like to express my sincere gratitude to all of you that, in different ways, have contributed to this work.

To my supervisor, *Michael Ljungberg*: Thank you for always seeing the opportunities rather than the obstacles, and for always trying to keep me on track.

To my co-supervisor, *Katarina Sjögreen Gleisner:* Thank you for your commitment and ability to see things from different angles.

To my assistant co-supervisor, colleague and former class-mate, *Johan Gustafsson*: Thank you for your willingness to always teach and share your knowledge.

To the former Ph.D. students at the Department of Medical Radiation Physics: Thank you for being good friends and colleagues, and congratulations on your well-earned Ph.D. degrees.

To the co-authors: Thank you for your valuable expertise, input, and rewarding collaboration that led to the publications included in this thesis.

To my other supporters: Thank you to all who, in different roles, over the last few years have encouraged and enabled me to finish my doctoral studies and to complete this thesis.

Thank you also to my past and present colleagues at the Department of Medical Radiation Physics, Lund University, and at the Nuclear Medicine unit, Radiation Physics, Skåne University Hospital.

To my family and my friends: Thank you for always being there. *Cecilia*, thank you for your endless support, tremendous work with our little boy, and for being who you are.

Support for this work was granted by the Swedish Research Council (ID 621-2014-6187), the Berta Kamprad Foundation, the Gunnar Nilsson Cancer Foundation, and the Swedish Cancer Foundation. Travel grants from the Swedish Society for Radiation Physics, John and Augusta Persson's Foundation, and the COMPUTE research school at Lund University are gratefully acknowledged.

References

1. SSM. *Swedish radiation safety authority*. 2015-02-01; Available from: https://www.stralsakerhetsmyndigheten.se/Yrkesverksam/Vard/Isotopstatistik/.
2. Starck, S. and Carlsson, S., *History of the Swedish society of nuclear medicine*, in *Nuclear medicine: Fusing the ideas of Democritus and Hippocrates - 25 years of the EANM*, E. Bombardieri and S. Frangos, Editors. 2012, European Association of Nuclear Medicine.
3. Starck, S. and Dahlén, U. *Survey SPECT/CT, PET/CT*. in *National meeting for medical physicists*. 2014.
4. Tucker, W.D., Greene, M.W., Weiss, A.J., and Murrenhoff, A., *Methods of preparation of some carrier-free radioisotopes involving sorption on alumina.* Transactions American Nuclear Society, 1958. **1**: p. 160:161.
5. Eckelman, W.C., *Unparalleled contribution of Technetium-99m to medicine over 5 decades.* JACC: Cardiovascular Imaging, 2009. **2**(3): p. 364-368.
6. Bajc, M., et al., *EANM guidelines for ventilation/perfusion scintigraphy : Part 1. Pulmonary imaging with ventilation/perfusion single photon emission tomography.* European Journal of Nuclear Medicine and Molecular Imaging, 2009. **36**(8): p. 1356-70.
7. Verberne, H.J., et al., *EANM procedural guidelines for radionuclide myocardial perfusion imaging with SPECT and SPECT/CT: 2015 revision.* European Journal of Nuclear Medicine and Molecular Imaging, 2015. **42**(12): p. 1929-1940.
8. Taylor, A. and Nally, J.V., *Clinical applications of renal scintigraphy.* American Journal of Roentgenology, 1995. **164**(1): p. 31-41.
9. Šámal, M. *Database of dynamic renal scintigraphy*. 2015-02-02; Available from: http://dynamicrenalstudy.org/.
10. Krenning, E.P., et al., *Localistation of endocrine-related tumours with radioiodinated analogue of somatostatin.* The Lancet, 1989. **333**(8632): p. 242-244.
11. Krenning, E.P., et al., *Somatostatin receptor scintigraphy with Indium-111-DTPA-D-Phe-1-Octreotide in man: Metabolism, dosimetry and comparison with Iodine-123-Tyr-3-Octreotide.* Journal of Nuclear Medicine, 1992. **33**(5): p. 652-658.
12. Krenning, E.P., et al., *Somatostatin receptor scintigraphy with [111In-DTPA-d-Phe1]- and [123I-Tyr3]-octreotide: the Rotterdam experience with more than 1000 patients.* European Journal of Nuclear Medicine, 1993. **20**(8): p. 716-731.
13. Krenning, E.P., et al., *Radiotherapy with a radiolabeled somatostatin analogue, [111In-DTPA-d-Phe1]-Octreotide.* Annals of the New York Academy of Sciences, 1994. **733**(1): p. 496-506.

14. Teunissen, J.J., Kwekkeboom, D.J., Valkema, R., and Krenning, E.P., *Nuclear medicine techniques for the imaging and treatment of neuroendocrine tumours.* Endocrine-Related Cancer, 2011. **18 Suppl 1**: p. S27-51.
15. Kwekkeboom, D.J., et al., *Treatment with the radiolabeled somatostatin analog [177Lu-DOTA0,Tyr3]Octreotate: Toxicity, efficacy, and survival.* Journal of Clinical Oncology, 2008. **26**(13): p. 2124-2130.
16. Bodei, L., et al., *Long-term evaluation of renal toxicity after peptide receptor radionuclide therapy with 90Y-DOTATOC and 177Lu-DOTATATE: the role of associated risk factors.* European Journal of Nuclear Medicine and Molecular Imaging, 2008. **35**(10): p. 1847-1856.
17. Strosberg, J., et al., *Phase 3 trial of 177Lu-Dotatate for midgut neuroendocrine tumors.* New England Journal of Medicine, 2017. **376**(2): p. 125-135.
18. Imhof, A., et al., *Response, survival, and long-term toxicity after therapy with the radiolabeled somatostatin analogue [90Y-DOTA]-TOC in metastasized neuroendocrine cancers.* Journal of Clinical Oncology, 2011. **29**(17): p. 2416-2423.
19. Valkema, R., et al., *Long-term follow-up of renal function after peptide receptor radiation therapy with 90Y-DOTA0,Tyr3-Octreotide and 177Lu-DOTA0, Tyr3-Octreotate.* Journal of Nuclear Medicine, 2005. **46**(1 suppl): p. 83S-91S.
20. Strigari, L., et al., *The evidence base for the use of internal dosimetry in the clinical practice of molecular radiotherapy.* European Journal of Nuclear Medicine and Molecular Imaging, 2014. **41**(10): p. 1976-1988.
21. Anger, H.O., *Scintillation camera.* Review of Scientific Instruments, 1958. **29**(1): p. 27-33.
22. Keidar, Z., Raysberg, I., Lugassi, R., Frenkel, A., and Israel, O., *Novel Cadmium Zinc Telluride based detector general purpose gamma camera: Initial evaluation and comparison with a standard camera.* Journal of Nuclear Medicine, 2016. **57**(supplement 2): p. 259.
23. Bocher, M., Blevis, I.M., Tsukerman, L., Shrem, Y., Kovalski, G., and Volokh, L., *A fast cardiac gamma camera with dynamic SPECT capabilities: design, system validation and future potential.* European Journal of Nuclear Medicine and Molecular Imaging, 2010. **37**(10): p. 1887-1902.
24. Gambhir, S.S., et al., *A novel high-sensitivity rapid-acquisition single-photon cardiac imaging camera.* Journal of Nuclear Medicine, 2009. **50**(4): p. 635-643.
25. Knoll, G.F., *Scintillation detector principles*, in *Radiation detection and measurement*. 2000, Wiley.
26. Dewaraja, Y.K., et al., *MIRD pamphlet No. 24: Guidelines for quantitative 131I SPECT in dosimetry applications.* Journal of Nuclear Medicine, 2013. **54**(12): p. 2182-8.
27. Berger, M.J., et al. *XCOM: Photon cross sections database, NIST standard reference database 8 (XGAM).* 2017 2017-06-22; Available from: https://www.nist.gov/pml/xcom-photon-cross-sections-database.
28. Jaszczak, R.J., Greer, K.L., Floyd, C.E., Harris, C.C., and Coleman, R.E., *Improved SPECT quantification using compensation for scattered photons.* Journal of Nuclear Medicine, 1984. **25**(8): p. 893-900.

29. Ogawa, K., Harata, Y., Ichihara, T., Kubo, A., and Hashimoto, S., *A practical method for position-dependent Compton-scatter correction in single photon emission CT.* IEEE Transactions on Medical Imaging, 1991. **10**(3): p. 408-412.
30. Koral, K.F., Swailem, F.M., Buchbinder, S., Clinthorne, N.H., Rogers, W.L., and Tsui, B.M.W., *SPECT dual-energy-window compton correction: Scatter multiplier required for quantification.* Journal of Nuclear Medicine, 1990. **31**(1): p. 90-98.
31. Fleming, J.S., *A technique for the absolute measurement of activity using a gamma camera and computer.* Physics in Medicine and Biology, 1979. **24**(1): p. 176.
32. Starck, S. and Carlsson, S., *The determination of the effective attenuation coefficient from effective organ depth and modulation transfer function in gamma camera imaging.* Physics in Medicine and Biology, 1997. **42**(10): p. 1957.
33. Wu, R.K. and Siegel, J.A., *Absolute quantitation of radioactivity using the buildup factor.* Medical Physics, 1984. **11**(2): p. 189-92.
34. Ljungberg, M. and Strand, S.-E., *Attenuation correction in SPECT based on transmission studies and Monte Carlo simulations of build-up functions.* Journal of Nuclear Medicine, 1990. **31**(4): p. 493-500.
35. Axelsson, B., Msaki, P., and Israelsson, A., *Subtraction of compton-scattered photons in single-photon emission computerized tomography.* Journal of Nuclear Medicine, 1984. **25**(4): p. 490-494.
36. Sjögreen, K., Ljungberg, M., and Strand, S.-E., *An activity quantification method based on registration of CT and whole-body scintillation camera images, with application to 131I.* Journal of Nuclear Medicine, 2002. **43**(7): p. 972-982.
37. Sjögreen Gleisner, K. and Ljungberg, M., *Patient-specific whole-body attenuation correction maps from a CT system for conjugate-view-based activity quantification: Method development and evaluation.* Cancer Biotherapy and Radiopharmaceuticals, 2012. **27**(10): p. 652-664.
38. Minarik, D., Sjögreen, K., and Ljungberg, M., *A new method to obtain transmission images for planar whole-body activity quantification.* Cancer Biotherapy and Radiopharmaceuticals, 2005. **20**(1): p. 72-76.
39. Tsui, B.M.W. and Frey, E.C., *Analytic image reconstruction methods in emission computed tomography*, in *Quantitative analysis in nuclear medicine imaging*, H. Zaidi, Editor. 2006, Springer US: Boston, MA. p. 82-106.
40. Hutton, B.F., Nuyts, J., and Zaidi, H., *Iterative reconstruction methods*, in *Quantitative analysis in nuclear medicine imaging*, H. Zaidi, Editor. 2006, Springer US. p. 107-140.
41. Shepp, L.A. and Vardi, Y., *Maximum likelihood reconstruction for emission tomography.* IEEE Transactions on Medical Imaging, 1982. **1**(2): p. 113-122.
42. Bruyant, P.P., *Analytic and iterative reconstruction algorithms in SPECT.* Journal of Nuclear Medicine, 2002. **43**(10): p. 1343-1358.
43. Gullberg, G.T., Huesman, R.H., Malko, J.A., Pelc, N.J., and Budinger, T.F., *An attenuated projector-backprojector for iterative SPECT reconstruction.* Physics in Medicine and Biology, 1985. **30**(8): p. 799-816.

44. Frey, E.C., Ju, Z.W., and Tsui, B.M.W., *A fast projector-backprojector pair modeling the asymmetric, spatially varying scatter response function for scatter compensation in SPECT imaging*. IEEE Transactions on Nuclear Science, 1993. **40**(4): p. 1192-1197.
45. Wells, R.G., Celler, A., and Harrop, R., *Analytical calculation of photon distributions in SPECT projections.* Nuclear Science, IEEE Transactions on, 1998. **45**(6): p. 3202-3214.
46. Beekman, F.J., Eijkman, E.G.J., Viergever, M.A., Borm, G.F., and Slijpen, E.T.P., *Object shape dependent PSF model for SPECT imaging.* IEEE Transactions on Nuclear Science, 1993. **40**(1): p. 31-39.
47. Frey, E.C. and Tsui, B. *A new method for modeling the spatially-variant, object-dependent scatter response function in SPECT*. in *Nuclear Science Symposium, 1996. Conference Record., 1996 IEEE*. 1996. IEEE.
48. Beekman, F.J., de Jong, H.W.A.M., and van Geloven, S., *Efficient fully 3-D iterative SPECT reconstruction with Monte Carlo-based scatter compensation.* IEEE Transactions on Medical Imaging, 2002. **21**(8): p. 867-877.
49. Hudson, H.M. and Larkin, R.S., *Accelerated image reconstruction using ordered subsets of projection data.* IEEE Transactions on Medical Imaging, 1994. **13**(4): p. 601-609.
50. Erlandsson, K., Buvat, I., Pretorius, P.H., Thomas, B.A., and Hutton, B.F., *A review of partial volume correction techniques for emission tomography and their applications in neurology, cardiology and oncology*. Physics in Medicine and Biology, 2012. **57**(21): p. R119-R159.
51. Frey, E.C. and Tsui, B.M.W., *Collimator-detector response compensation in SPECT*, in *Quantitative analysis in nuclear medicine imaging*, H. Zaidi, Editor. 2006, Springer US. p. 141-166.
52. Tsui, B.M.W., Hu, H.B., Gilland, D.R., and Gullberg, G.T., *Implementation of simultaneous attenuation and detector response correction in SPECT.* IEEE Transactions on Nuclear Science, 1988. **35**(1): p. 778-783.
53. Yong, D., Tsui, B.M.W., and Frey, E.C., *Partial volume effect compensation for quantitative brain SPECT imaging.* IEEE Transactions on Medical Imaging, 2005. **24**(8): p. 969-976.
54. Zeintl, J., Vija, A.H., Yahil, A., Hornegger, J., and Kuwert, T., *Quantitative accuracy of clinical 99mTc SPECT/CT using ordered-subset expectation maximization with 3-dimensional resolution recovery, attenuation, and scatter correction.* Journal of Nuclear Medicine, 2010. **51**(6): p. 921-8.
55. Ljungberg, M., *Introduction to the Monte Carlo method*, in *Monte Carlo calculations in nuclear medicine, second edition*. 2012, Taylor & Francis. p. 1-16.
56. Salvat, F., Fernandez-Varea, J.M., and Sempau, J. *PENELOPE-2011, A code system for Monte Carlo simulation of electron and photon transport*. in *PENELOPE Workshop 2011*. 2011. Barcelona, Spain: OECD Nuclear Energy Agency.
57. Jan, S., et al., *GATE: a simulation toolkit for PET and SPECT.* Physics in Medicine and Biology, 2004. **49**(19): p. 4543.

58. Munck af Rosenschöld, P. and Larsson, E., *The MCNP Monte Carlo program*, in *Monte Carlo calculations in nuclear medicine, second edition*. 2012, Taylor & Francis. p. 153-172.
59. Wilderman, S.J. and Namito, Y., *The EGS family of code systems*, in *Monte Carlo calculations in nuclear medicine, second edition*. 2012, Taylor & Francis. p. 173-200.
60. Ljungberg, M., *The SIMIND Monte Carlo program*, in *Monte Carlo calculations in nuclear medicine, second edition*. 2012, Taylor & Francis. p. 111-128.
61. Ljungberg, M. and Strand, S.E., *A Monte Carlo program for the simulation of scintillation camera characteristics.* Computer Methods and Programs in Biomedicine, 1989. **29**(4): p. 257-272.
62. Ljungberg, M., *SIMIND Monte Carlo based image reconstruction.* Journal of Nuclear Medicine, 2015. **56**(supplement 3): p. 43.
63. Pretorius, P.H., Liu, C., Fan, P., Peterson, M., and Ljungberg, M., *Monte Carlo simulations of the GE Discovery Alcyone CZT SPECT systems.* IEEE Transactions on Nuclear Science, 2015. **62**(3): p. 832-839.
64. Nelson, W.R., Hirayama, H., and Rogers, D.W.O., *The EGS4 code system*. 1985: Standford, California, USA.
65. Hindorf, C., Ljungberg, M., and Strand, S.-E., *Evaluation of parameters influencing S values in mouse dosimetry.* Journal of Nuclear Medicine, 2004. **45**(11): p. 1960-1965.
66. Segars, W.P., Tsui, B.M.W., Frey, E.C., Johnson, G.A., and Berr, S.S., *Development of a 4-D digital mouse phantom for molecular imaging research.* Molecular Imaging and Biology, 2004. **6**(3): p. 149-159.
67. Snyder, W.S., Fisher, H.L., Jr., Ford, M.R., and Warner, G.G., *Estimates of absorbed fractions for monoenergetic photon sources uniformly distributed in various organs of a heterogeneous phantom.* Journal of Nuclear Medicine, 1969: p. Suppl 3:7-52.
68. Zubal, I.G., Harrell, C.R., Smith, E.O., Rattner, Z., Gindi, G., and Hoffer, P.B., *Computerized three-dimensional segmented human anatomy.* Medical Physics, 1994. **21**(2): p. 299-302.
69. ICRP, *Adult reference computational phantoms. ICRP publication 110.* Annals of the ICRP, 2009. **39**(2).
70. Lee, C., Williams, J.L., Lee, C., and Bolch, W.E., *The UF series of tomographic computational phantoms of pediatric patients.* Medical Physics, 2005. **32**(12): p. 3537-3548.
71. Segars, W.P. and Tsui, M.W., *The MCAT, NCAT, XCAT, and MOBY computational human and mouse phantoms*, in *Handbook of anatomical models for radiation dosimetry*. 2009, Taylor & Francis. p. 105-133.
72. Segars, W.P., Sturgeon, G., Mendonca, S., Grimes, J., and Tsui, B.M.W., *4D XCAT phantom for multimodality imaging research.* Medical Physics, 2010. **37**(9): p. 4902-4915.
73. *Visible human male and female datasets, National library of medicine*. Available from: http://www.nlm.nih.gov/research/visible/visible_human.html.

74. Segars, W.P., et al., *Population of anatomically variable 4D XCAT adult phantoms for imaging research and optimization.* Medical Physics, 2013. **40**(4): p. 043701.
75. Lee, C., Lodwick, D., Hurtado, J., Pafundi, D., Williams, J.L., and Bolch, W.E., *The UF family of reference hybrid phantoms for computational radiation dosimetry.* Physics in medicine and biology, 2010. **55**(2): p. 339-363.
76. Choonsik, L., Daniel, L., Deanna, H., Jonathan, L.W., Choonik, L., and Wesley, E.B., *Hybrid computational phantoms of the male and female newborn patient: NURBS-based whole-body models.* Physics in Medicine and Biology, 2007. **52**(12): p. 3309.
77. Matthew , R.M., et al., *The UF Family of hybrid phantoms of the pregnant female for computational radiation dosimetry.* Physics in Medicine and Biology, 2014. **59**(15): p. 4325.
78. Nickel, M., Strand, S.-E., Lindén, O., Wingårdh, K., Tennwall, J., and Gleisner, K.S., *Development and evaluation of a pharmacokinetic model for prediction of radioimmunotherapy based on pretherapy data.* Cancer Biotherapy and Radiopharmaceuticals, 2009. **24**(1): p. 111-122.
79. Phelps, M.E., Huang, S.C., Hoffman, E.J., Selin, C., Sokoloff, L., and Kuhl, D.E., *Tomographic measurement of local cerebral glucose metabolic rate in humans with (F-18)2-fluoro-2-deoxy-D-glucose: Validation of method.* Annals of Neurology, 1979. **6**(5): p. 371-388.
80. Blaufox, M.D., Potchen, E.J., and Merrill, J.P., *Measurement of effective renal plasma flow in man by external counting methods.* Journal of Nuclear Medicine, 1967. **8**(2): p. 77-85.
81. Farde, L., Eriksson, L., Blomquist, G., and Halldin, C., *Kinetic analysis of central [11C]raclopride binding to D2-dopamine receptors studied by PET - A comparison to the equilibrium analysis.* Journal of Cerebral Blood Flow and Metabolism, 1989. **9**(5): p. 696-708.
82. Press, W.H., Teukolsky, S.A., Vetterling, W.T., and Flannery, B.P., *Numerical recipes in C: The art of scientific computing.* Second ed. 1992, New York, NY, USA: Cambridge University Press.
83. Ozasa, K., et al., *Studies of the mortality of atomic bomb survivors, Report 14, 1950–2003: an overview of cancer and noncancer diseases.* Radiation research, 2011. **177**(3): p. 229-243.
84. ICRP, *Low-dose extrapolation of radiation-related cancer risk. ICRP Publication 99.* Annals of the ICRP, 2005. **35**(4).
85. Siegel, J.A., Pennington, C.W., and Sacks, B., *Subjecting radiological imaging to the linear no-threshold hypothesis: A non sequitur of non-trivial proportion.* Journal of Nuclear Medicine, 2016.
86. Andersson, M., *Erratum to: Effective dose to adult patients from 338 radiopharmaceuticals estimated using ICRP biokinetic data, ICRP/ICRU computational reference phantoms and ICRP 2007 tissue weighting factors.* EJNMMI Physics, 2015. **2**: p. 22.
87. Andersson, M., Johansson, L., Minarik, D., Leide-Svegborn, S., and Mattsson, S., *Effective dose to adult patients from 338 radiopharmaceuticals estimated using ICRP*

biokinetic data, ICRP/ICRU computational reference phantoms and ICRP 2007 tissue weighting factors. EJNMMI Physics, 2014. **1**: p. 9.

88. Bolch, W.E., Eckerman, K.F., Sgouros, G., and Thomas, S.R., *MIRD Pamphlet No. 21: A generalized schema for radiopharmaceutical dosimetry - Standardization of nomenclature.* Journal of Nuclear Medicine, 2009. **50**(3): p. 477-484.
89. Minarik, D., Sjögreen Gleisner, K., and Ljungberg, M., *Evaluation of quantitative 90Y SPECT based on experimental phantom studies.* Physics in Medicine and Biology, 2008. **53**(20): p. 5689.
90. Dewaraja, Y.K., et al., *MIRD Pamphlet No. 23: Quantitative SPECT for patient-specific 3-dimensional dosimetry in internal radionuclide therapy.* Journal of Nuclear Medicine, 2012. **53**(8): p. 1310-1325.
91. Fritzberg, A.R., Kasina, S., Eshima, D., and Johnson, D.L., *Synthesis and biological evaluation of Technetium-99m MAG3 as a hippuran replacement.* Journal of Nuclear Medicine, 1986. **27**(1): p. 111-116.
92. Taylor, A., Eshima, D., Christian, P.E., Wooten, W.W., Hansen, L., and McElvany, K., *Technetium-99m MAG3 kit formulation: Preliminary results in normal volunteers and patients with renal failure.* Journal of Nuclear Medicine, 1988. **29**(5): p. 616-622.
93. Prigent, A., et al., *Consensus report on quality control of quantitative measurements of renal function obtained from the renogram: International consensus committee from the scientific committee of radionuclides in nephrourology.* Seminars in Nuclear Medicine, 1999. **29**(2): p. 146-59.
94. Fleming, J.S. and Kemp, P.M., *A comparison of deconvolution and the Patlak-Rutland plot in renography analysis.* Journal of Nuclear Medicine, 1999. **40**(9): p. 1503-1507.
95. Rutland, M.D., *A comprehensive analysis of renal DTPA studies. I. Theory and normal values.* Nuclear Medicine Communications, 1985. **6**(1): p. 11-20.
96. Wesolowski, M.J., et al., *A simple method for determining split renal function from dynamic (99m)Tc-MAG3 scintigraphic data.* European Journal of Nuclear Medicine and Molecular Imaging, 2016. **43**(3): p. 550-8.
97. Taylor, A., et al., *Measuring Technetium-99m-MAG3 clearance with an improved camera-based method.* Journal of Nuclear Medicine, 1995. **36**(9): p. 1689-1695.
98. Gates, G.F., *Glomerular filtration rate: estimation from fractional renal accumulation of 99mTc-DTPA (stannous).* American Journal of Roentgenology, 1982. **138**(3): p. 565-570.
99. Schlegel, J.U., Halikiopoulos, H.L., and Prima, R., *Determination of filtration fraction using the gamma scintillation camera.* Journal of Urology, 1979. **122**(4): p. 447-50.
100. Taylor, A., Lewis, C., Giacometti, A., Hall, E.C., and Barefield, K.P., *Improved formulas for the estimation of renal depth in adults.* Journal of Nuclear Medicine, 1993. **34**(10): p. 1766-1769.
101. Sjögreen, K., Ljungberg, M., Wingardh, K., Minarik, D., and Strand, S.E., *The LundADose method for planar image activity quantification and absorbed-dose*

assessment in radionuclide therapy. Cancer Biotherapy and Radiopharmaceuticals, 2005. **20**(1): p. 92-7.

102. Bubeck, B., Brandau, W., Weber, E., Kälble, T., Parekh, N., and Georgi, P., *Pharmacokinetics of Technetium-99m-MAG3 in humans.* Journal of Nuclear Medicine, 1990. **31**(8): p. 1285-1293.
103. Russell, C.D., *A Bayesian 3-compartment model for 99mTc-MAG3 clearance.* Journal of Nuclear Medicine, 2003. **44**(8): p. 1357-1361.
104. Itoh, K., *99mTc-MAG3: review of pharmacokinetics, clinical application to renal diseases and quantification of renal function.* Annals of Nuclear Medicine, 2001. **15**(3): p. 179-90.
105. Taylor, A.T., Lipowska, M., and Marzilli, L.G., *(99m)Tc(CO)(3)(NTA): A (99m)Tc renal tracer with pharmacokinetic properties comparable to those of (131)I-OIH in healthy volunteers.* Journal of Nuclear Medicine, 2010. **51**(3): p. 391-396.
106. Rehling, M., Nielsen, B.V., Pedersen, E.B., Nielsen, L.E., Hansen, H.E., and Bacher, T., *Renal and extrarenal clearance of 99mTc-MAG3: A comparison with 125I-OIH and 51Cr-EDTA in patients representing all levels of glomerular filtration rate.* European Journal of Nuclear Medicine, 1995. **22**(12): p. 1379-1384.
107. Durand, E., et al., *International scientific committee of radionuclides in nephrourology (ISCORN) consensus on renal transit time measurements.* Seminars in Nuclear Medicine, 2008. **38**(1): p. 82-102.
108. Esteves, F.P., Taylor, A., Manatunga, A., Folks, R.D., Krishnan, M., and Garcia, E.V., *99mTc-MAG3 renography: Normal values for MAG3 clearance and curve parameters, excretory parameters, and residual urine volume.* American Journal of Roentgenology, 2006. **187**(6): p. W610-W617.
109. Russell, C.D., Taylor, A.T., and Dubovsky, E.V., *A Bayesian regression model for plasma clearance.* Journal of Nuclear Medicine, 2002. **43**(6): p. 762-766.
110. *Equalis*. Available from: http://www.equalis.se/en/products-and-services/external-quality-assessment-eqa/eqa-areas-advisory-groups/nuclear-medicine.aspx.
111. Sandstrom, M., et al., *Individualized dosimetry of kidney and bone marrow in patients undergoing 177Lu-DOTA-octreotate treatment.* Journal of Nuclear Medicine, 2013. **54**(1): p. 33-41.
112. Guerriero, F., et al., *Kidney dosimetry in 177Lu and 90Y peptide receptor radionuclide therapy: influence of image timing, time-activity integration method, and risk factors.* Biomed Research International, 2013. **2013**: p. 935351.
113. Ljungberg, M., et al., *MIRD Pamphlet No. 26: Joint EANM/MIRD guidelines for quantitative 177Lu SPECT applied for dosimetry of radiopharmaceutical therapy.* Journal of Nuclear Medicine, 2016. **57**(1): p. 151-62.
114. Kwekkeboom, D., et al., *[177Lu-DOTA0,Tyr3]octreotate: comparison with [111In-DTPA0]octreotide in patients.* European Journal of Nuclear Medicine, 2001. **28**(9): p. 1319-1325.
115. Esser, J.P., et al., *Comparison of [177Lu-DOTA0,Tyr3]octreotate and [177Lu-DOTA0,Tyr3]octreotide: which peptide is preferable for PRRT?* European Journal of Nuclear Medicine and Molecular Imaging, 2006. **33**(11): p. 1346-1351.

116. Melis, M., Krenning, E., Bernard, B., Barone, R., Visser, T., and Jong, M., *Localisation and mechanism of renal retention of radiolabelled somatostatin analogues.* European Journal of Nuclear Medicine and Molecular Imaging, 2005. **32**(10): p. 1136-1143.

117. Rolleman, E., Melis, M., Valkema, R., Boerman, O., Krenning, E., and Jong, M., *Kidney protection during peptide receptor radionuclide therapy with somatostatin analogues.* European Journal of Nuclear Medicine and Molecular Imaging, 2010. **37**(5): p. 1018-1031.

118. Ljungberg, M., Sjögreen, K., Liu, X., Frey, E., Dewaraja, Y., and Strand, S.-E., *A 3-dimensional absorbed dose calculation method based on quantitative SPECT for radionuclide therapy: Evaluation for (131)I using Monte Carlo simulation.* Journal of Nuclear Medicine, 2002. **43**(8): p. 1101-1109.

119. Liu, X., Ljungberg, M., and Strand, S.E., *DOSIMG: a 3D voxel-based Monte Carlo program for absorbed dose calculations [abstract]*. Journal of Nuclear Medicine, 2001. **42**(Suppl): p. 243P.

120. Stabin, M.G., Sparks, R.B., and Crowe, E., *OLINDA/EXM: The second-generation personal computer software for internal dose assessment in nuclear medicine.* Journal of Nuclear Medicine, 2005. **46**(6): p. 1023-1027.

121. Garkavij, M., et al., *177Lu-[DOTA0,Tyr3] octreotate therapy in patients with disseminated neuroendocrine tumors: Analysis of dosimetry with impact on future therapeutic strategy*. Cancer, 2010. **116**(4 Suppl): p. 1084-92.

122. He, B. and Frey, E.C., *The impact of 3D volume of interest definition on accuracy and precision of activity estimation in quantitative SPECT and planar processing methods.* Physics in Medicine and Biology, 2010. **55**(12): p. 3535.

123. He, B., et al., *Evaluation of quantitative imaging methods for organ activity and residence time estimation using a population of phantoms having realistic variations in anatomy and uptake.* Medical Physics, 2009. **36**(2): p. 612-619.

124. Anizan, N., Wang, H., Zhou, X.C., Hobbs, R.F., Wahl, R.L., and Frey, E.C., *Factors affecting the stability and repeatability of gamma camera calibration for quantitative imaging applications based on a retrospective review of clinical data.* EJNMMI Research, 2014. **4**: p. 67.

125. Anizan, N., Wang, H., Zhou, X.C., Wahl, R.L., and Frey, E.C., *Factors affecting the repeatability of gamma camera calibration for quantitative imaging applications using a sealed source.* Physics in Medicine and Biology, 2015. **60**(3): p. 1325-1337.

126. Delker, A., et al., *The influence of early measurements onto the estimated kidney dose in [(177)Lu][DOTA(0),Tyr(3)]Octreotate peptide receptor radiotherapy of neuroendocrine tumors.* Molecular Imaging and Biology, 2015. **17**(5): p. 726-34.

127. Bakker, W.H., Breeman, W.A., Kwekkeboom, D.J., De Jong, L.C., and Krenning, E.P., *Practical aspects of peptide receptor radionuclide therapy with [177Lu][DOTA0, Tyr3]octreotate.* The Quarterly Journal of Nuclear Medicine and Molecular Imaging, 2006. **50**(4): p. 265-71.

128. Zhang, J.L., Rusinek, H., Chandarana, H., and Lee, V.S., *Functional MRI of the kidneys.* Journal of magnetic resonance imaging, 2013. **37**(2): p. 282-293.

129. Nijran, K.S., et al., *UK audit of analysis of quantitative parameters from renography data generated using a physical phantom.* Nuclear Medicine Communications, 2014. **35**(7): p. 745-754.
130. Nykänen, A.O., Rautio, P.J., Aarnio, J.V., and Heikkinen, J.O., *Multicenter evaluation of renography with an automated physical phantom.* Nuclear Medicine Communications, 2014. **35**(9): p. 977-984.
131. MetroMRT. *Metrology for molecular radiation therapy*. Available from: http://projects.npl.co.uk/metromrt/.
132. Garcia, M.-P., et al., *TestDose: A nuclear medicine software based on Monte Carlo modeling for generating gamma camera acquisitions and dosimetry.* Medical Physics, 2015. **42**(12): p. 6885-6894.
133. Brolin, G., Sjögreen Gleisner, K., Gustafsson, J., and Ljungberg, M., *Evaluation of template-based partial volume correction methods in 177Lu SPECT imaging for dosimetry improvement in peptide receptor radionuclide therapy (abstract P0028).* European Journal of Nuclear Medicine, 2012. **39**(Suppl. 2): p. 304-353.

Appendix 1: Activity quantification in planar imaging

Single projection

Following equation (1), a parallel planar projection count-rate distribution image $p(x,y)$ along the positive z–axis is given by:

$$p(x,y) = \varepsilon_{air} \cdot \int_{z_{min}(x,y)}^{z_{max}(x,y)} f(x,y,z) \exp\left[-\int_{z}^{z_{\max}(x,y)} \mu(x,y,z')dz'\right] dz \ , \qquad \text{(A1.1)}$$

where ε_{air} is the camera sensitivity, $f(x,y,z)$ is the 3D activity distribution, $\mu(x,y,z)$ is the 3D distribution of linear attenuation coefficients, and $z_{min}(x,y)$ and $z_{max}(x,y)$ are the patient boundary coordinates farthest from and closest to the camera head, respectively, both at position (x,y). Note that equation (A1.1) is valid only for a narrow-beam geometry without contribution from scattered photons, and with perfect spatial resolution, i.e., perfect parallel collimation along the z-axis. The count rate R in a ROI is thus the 2D integral of the projection image over the ROI area:

$$R = \iint_{ROI} p(x,y)dxdy \ = \qquad \text{(A1.2)}$$

$$= \varepsilon_{air} \iint_{ROI} \left\{ \int_{z_{\min}(x,y)}^{z_{\max}(x,y)} f(x,y,z) \exp\left[-\int_{z}^{z_{\max}(x,y)} \mu(x,y,z')dz'\right] dz \right\} dxdy \ .$$

Assuming that the source has an infinitesimal extension in the z–direction, i.e., that $f(x,y,z) = g(x,y)\delta(z - z_o(x,y))$ where δ denotes the Dirac delta function, equation (A1.2) becomes:

$$R = \varepsilon_{\text{air}} \iint_{ROI} \left\{ g(x,y) \exp\left[- \int_{z_0(x,y)}^{z_{\max(x,y)}} \mu(x,y,z')dz' \right] \right\} dxdy \,. \tag{A1.3}$$

Define a 2D attenuation distribution $\mathrm{M}(x,y)$ according to

$$\mathrm{M}(x,y) = \exp\left[- \int_{z_0(x,y)}^{z_{\max(x,y)}} \mu(x,y,z')dz' \right], \tag{A1.4}$$

so that equation (A1.4) becomes

$$R = \varepsilon_{\text{air}} \iint_{ROI} g(x,y) \cdot \mathrm{M}(x,y)dxdy. \tag{A1.5}$$

If the attenuation distribution is uniform over the ROI, i.e., $\mathrm{M}(x,y) = \mathrm{M}, \forall (x,y) \in ROI$, equation (A1.5) is further simplified to

$$R = \varepsilon_{air} \mathrm{M} \iint_{ROI} g(x,y)dxdy, \tag{A1.6}$$

and noting that $A_{ROI} = \iint_{ROI} g(x,y)dxdy$ is the activity contained in the ROI, we may write

$$R = \varepsilon_{\text{air}} \cdot A_{ROI} \cdot \mathrm{M} \,. \tag{A1.7}$$

The assumption of a uniform attenuation over the ROI is justified if the source is located at a well-defined depth in a uniform medium, i.e., that $z_{\max}(x,y) - z_0(x,y) = d$ and $\mu(x,y,z) = \mu, \forall\, (x,y) \in ROI$. Then, equation (A1.4) becomes $\mathrm{M} = e^{-\mu d}$ for all points in the ROI, and the count rate according to equation (A1.7) is in agreement with equation (2):

$$R = \varepsilon_{\text{air}} \cdot A_{ROI} \cdot e^{-\mu d} \,. \tag{A1.8}$$

Conjugate view

The conjugate-view method relies on acquisition of two opposing projection images, often anterior and posterior projections as illustrated in figure A1.1. Using equation (A1.1), the anterior projection $p_a(x,y)$ is given by:

$$p_a(x,y) = \varepsilon_{air} \cdot \int_{z_{\min}(x,y)}^{z_{\max}(x,y)} f(x,y,z) \exp\left[-\int_{z}^{z_{\max}(x,y)} \mu(x,y,z')dz'\right] dz \ , \qquad \text{(A1.9)}$$

and the posterior projection $p_p(x,y)$ by:

$$p_p(x,y) = \varepsilon_{\text{air}} \cdot \int_{z_{\min}(x,y)}^{z_{\max}(x,y)} f(x,y,z) \exp\left[-\int_{z_{\min}(x,y)}^{z} \mu(x,y,z')dz'\right] dz \ . \qquad \text{(A1.10)}$$

Following the assumptions used to derive equation (A1.8), the anterior and posterior ROI count rates R_a and R_p become

$$\begin{cases} R_a = \varepsilon_{\text{air}} \cdot A_{ROI} \cdot e^{-\mu d_a} \\ R_p = \varepsilon_{\text{air}} \cdot A_{ROI} \cdot e^{-\mu d_p} \end{cases} , \qquad \text{(A1.11)}$$

where $d_a = z_{\max}(x,y) - z_0(x,y)$ and $d_p = z_0(x,y) - z_{min}(x,y)$ are the anterior and posterior depth of the source, respectively, again assumed to be constant for all (x,y)-positions in the ROI. The geometric mean count rate is thus equal to:

$$\sqrt{R_a R_p} = \varepsilon_{\text{air}} \cdot A_{ROI} \cdot e^{-\frac{\mu}{2}(d_a+d_p)} = \varepsilon_{\text{air}} \cdot A_{ROI} \cdot e^{-\frac{\mu T}{2}} , \qquad \text{(A1.12)}$$

where $T = d_a + d_p$ is the patient thickness along the z-axis at the position of the ROI. The pixel-based implementation of the conjugate-view method is based on forming the geometric mean count-rate image $p_{GM}(x,y)$ following:

$$p_{GM}(x,y) = \left(p_a(x,y) \cdot p_p(x,y)\right)^{\frac{1}{2}} , \qquad \text{(A1.13)}$$

Inserting the expressions for $p_a(x,y)$ and $p_p(x,y)$, equation (A1.13) gives

$$
\begin{aligned}
&p_{GM}(x,y) \\
&= \varepsilon_{air} \left\{ \int_{z_{\min}(x,y)}^{z_{\max}(x,y)} f(x,y,z) \exp\left(- \int_{z}^{z_{\max}(x,y)} \mu(x,y,z')\mathrm{d}z' \right) \mathrm{d}z \right. \\
&\left. \cdot \int_{z_{\min}(x,y)}^{z_{\max}(x,y)} f(x,y,z) \exp\left(- \int_{z_{\min}(x,y)}^{z} \mu(x,y,z')\mathrm{d}z' \right) \mathrm{d}z \right\}^{\frac{1}{2}} .
\end{aligned}
\tag{A1.14}
$$

Once again assuming that $f(x,y,z) = g(x,y)\delta(z - z_o(x,y))$, (A1.14) gives:

$$
\begin{aligned}
&p_{GM}(x,y) = \\
&= \varepsilon_{0\mathrm{air}}\, g(x,y) \left\{ \exp\left(- \int_{z_0}^{z_{\max}(x,y)} \mu(x,y,z')\mathrm{d}z' \right) \exp\left(- \int_{z_{\min}(x,y)}^{z_0} \mu(x,y,z')\mathrm{d}z' \right) \mathrm{d}z \right\}^{\frac{1}{2}} \\
&= \varepsilon_{\mathrm{air}}\, g(x,y) \exp\left(-\frac{1}{2} \int_{z_{\min}(x,y)}^{z_{\max}(x,y)} \mu(x,y,z')\mathrm{d}z' \right),
\end{aligned}
\tag{A1.15}
$$

which is equivalent to

$$
g(x,y) = \varepsilon_{\mathrm{air}}^{-1} \cdot p_{GM}(x,y) \exp\left(\frac{1}{2} \int_{z_{\min}(x,y)}^{z_{\max}(x,y)} \mu(x,y,z)\mathrm{d}z \right). \tag{A1.16}
$$

Integrating both sides over the ROI and again using $A_{ROI} = \iint_{ROI} g(x,y)dxdy$, equation (A1.16) gives

$$
A_{ROI} = \varepsilon_{air}^{-1} \cdot \iint_{ROI} \left\{ p_{GM}(x,y) \exp\left(\frac{1}{2} \int_{z_{\min}(x,y)}^{z_{\max}(x,y)} \mu(x,y,z)\mathrm{d}z \right) \right\} dxdy\,, \tag{A1.17}
$$

in agreement with equation (8).

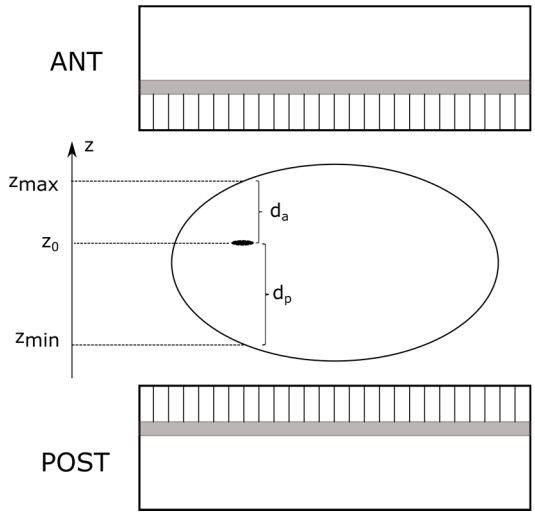

Figure A1.1. A radioactive source in a patient, located at coordinate z_0 on the z-axis (posterior-anterior direction), at depths d_a and d_p from the anterior and posterior skin surface, respectively.

Appendix 2: Clearance derivation in the two-compartment model

Clearance calculations for renal tracers, such as ^{99m}Tc-MAG3, are commonly based on a two-compartment model, owing to the observed bi-exponential plasma time-activity curve. The central compartment represents an initial distribution volume V_1, and the concentration of the tracer as a function of time can be sampled by repeated measurements of the activity concentration in plasma after administration. The central compartment is cleared by the kidneys (for an ideal renal tracer), as represented by the transfer rate constant k_{10}. The second, or peripheral, compartment represents the remaining volume of distribution in which the tracer is unavailable for excretion. The inter-compartmental exchange is represented by the transfer rate constants k_{12} and k_{21}.

Following equation (14), the two-compartment model depicted in figure 7 is described by

$$\frac{dA_1(t)}{dt} = k_{21}A_2(t) - (k_{12} + k_{10})A_1(t), \tag{A2.1}$$

and

$$\frac{dA_2(t)}{dt} = k_{12}A_1(t) - k_{21}A_2(t), \tag{A2.2}$$

where $A_1(t)$ and $A_2(t)$ are the amounts of tracer contained in the central and peripheral compartment, respectively. These equations constitute a system of linear first-order differential equations, which can be readily solved by numerical methods, such as the RK4 algorithm. An analytical solution may be useful in some cases, and can be obtained by means of the Laplace transform. If $\mathcal{L}$ represents the Laplace-transform operator, and a tilde denotes the Laplace-domain function with independent variable s, equation (A2.1) can be written as

$$\mathcal{L}\left(\frac{dA_1(t)}{dt}\right) = \mathcal{L}(k_{21}A_2(t) - (k_{12} + k_{10})A_1(t)) \Leftrightarrow$$

$$s\tilde{A}_1(s) - A_1(0) = k_{21}\tilde{A}_2(s) - (k_{12} + k_{10})\tilde{A}_1(s) \Leftrightarrow$$

$$\tilde{A}_1(s) = \frac{k_{21}\tilde{A}_2(s) + A_1(0)}{s + k_{12} + k_{10}}. \quad \text{(A2.3)}$$

Similarly, the Laplace transform of $A_2(t)$ is obtained from equation (A2.2) according to

$$\tilde{A}_2(s) = \frac{k_{12}\tilde{A}_1(s) + A_2(0)}{s + k_{21}}. \quad \text{(A2.4)}$$

Assuming that the tracer is administered as a bolus injection in the central compartment, the boundary conditions are $A_1(0) = N$ (the injected amount, e.g., in units of mole or MBq) and $A_2(0) = 0$. Using these when inserting equation (A2.4) into equation (A2.3) and rearranging terms, we get the following expression for $\tilde{A}_1(s)$:

$$\tilde{A}_1(s) = \frac{N(s + k_{21})}{s^2 + s(k_{12} + k_{21} + k_{10}) + k_{21}k_{10}}. \quad \text{(A2.5)}$$

Substituting the expression for $\tilde{A}_1(s)$ in equation (A2.4), we obtain

$$\tilde{A}_2(s) = \frac{k_{12}N}{s^2 + s(k_{12} + k_{21} + k_{10}) + k_{21}k_{10}}. \quad \text{(A2.6)}$$

The solutions to equations (A2.1) and (A2.2) can be obtained from the inverse Laplace transform of equations (A2.5) and (A2.6), respectively. To find the inverse Laplace transform, we rewrite equations (A2.5) and (A2.6) using partial fraction expansion. First, the denominator polynomial is factorised:

$$s^2 + s(k_{12} + k_{21} + k_{10}) + k_{21}k_{10} = (s - s_1)(s - s_2),$$

where

$$s_{1,2} = -\frac{k_{12} + k_{21} + k_{10}}{2} \pm \sqrt{\frac{1}{4}(k_{12} + k_{21} + k_{10})^2 - k_{21}k_{10}} \equiv -\lambda_{2,1}, \quad \text{(A2.7)}$$

so that equation (A2.5) may be written as

$$\tilde{A}_1(s) = \frac{N(s + k_{21})}{(s + \lambda_1)(s + \lambda_2)} = \frac{c_1}{s + \lambda_1} + \frac{c_2}{s + \lambda_2}, \qquad \text{(A2.8)}$$

where the coefficients c_1 and c_2 are given by

$$\begin{cases} c_1 + c_2 = N \\ c_1\lambda_2 + c_2\lambda_1 = Nk_{21} \end{cases} \Leftrightarrow \begin{cases} c_1 = \dfrac{N(\lambda_1 - k_{21})}{\lambda_1 - \lambda_2} \\ c_2 = \dfrac{N(\lambda_2 - k_{21})}{\lambda_2 - \lambda_1} \end{cases}.$$

Inserting the expressions for c_1 and c_2 in equation (A2.8), the Laplace transform of $A_1(t)$ becomes

$$\tilde{A}_1(s) = \frac{N}{\lambda_2 - \lambda_1}\left(\frac{k_{21} - \lambda_1}{s + \lambda_1} + \frac{\lambda_2 - k_{21}}{s + \lambda_2}\right). \qquad \text{(A2.9)}$$

The inverse Laplace transform, $\mathcal{L}^{-1}$, of equation (A2.9) yields the time-activity curve of the central compartment as a bi-exponential function with slope λ_1 and λ_2:

$$A_1(t) = \mathcal{L}^{-1}\left(\tilde{A}_1(s)\right) = \frac{N}{\lambda_2 - \lambda_1}\left((k_{21} - \lambda_1)e^{-\lambda_1 t} + (\lambda_2 - k_{21})e^{-\lambda_2 t}\right), \qquad \text{(A2.10)}$$

since the Laplace transform and its inverse are linear operators and $\mathcal{L}^{-1}\left(\frac{1}{s+a}\right) = e^{-at}$, where a denotes a constant. The expression for $A_2(t)$ can be derived in the same manner starting from equation (A2.6), and yields

$$A_2(t) = \mathcal{L}^{-1}\left(\tilde{A}_2(s)\right) = N\frac{k_{12}}{\lambda_2 - \lambda_1}\left(e^{-\lambda_1 t} - e^{-\lambda_2 t}\right). \qquad \text{(A2.11)}$$

The resulting time-activity curves are shown in figure A1, assuming typical values for ^{99m}Tc-MAG3 in normal subjects (k_{10} = 0.07 min^{-1}, $k_{12} = k_{21}$ = 0.16 min^{-1}).

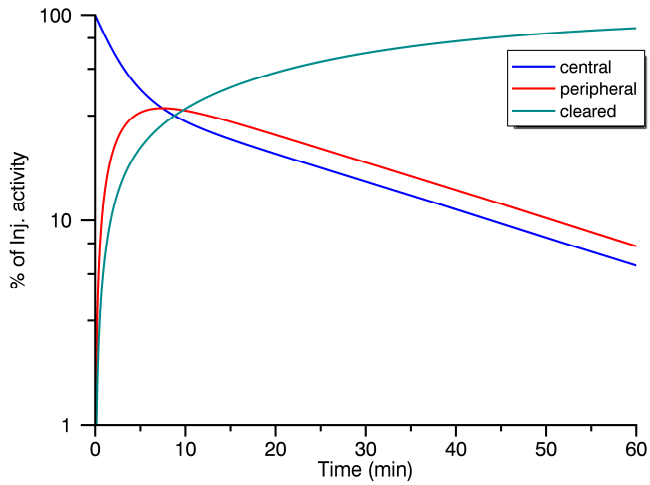

Figure A1. Typical time-activity curves in the central and peripheral compartment after injection of ^{99m}Tc-MAG3 in normal subjects. The dark cyan line represents the amount of tracer that has been cleared from the system due to renal excretion.

Clearance calculations for MAG3 (and other tracers exhibiting bi-exponential kinetics) following a single intravenous injection can be performed by sampling the tracer concentration in plasma and fitting a bi-exponential function to the data. The observed concentration curve is the time-activity curve of the central compartment divided by its volume:

$$C_1(t) = \frac{A_1(t)}{V_1}. \qquad \text{(A2.12)}$$

Substituting $a = \frac{N(k_{21}-\lambda_1)}{V_1(\lambda_2-\lambda_1)}$ and $b = \frac{N(\lambda_2-k_{21})}{V_1(\lambda_2-\lambda_1)}$ in equation (A2.10) and inserting in (A2.12), we obtain

$$C_1(t) = ae^{-\lambda_1 t} + be^{-\lambda_2 t} \qquad \text{(A2.13)}$$

Assuming that the macroconstants a, b, λ_1, and λ_2 can be estimated by model fitting, the transfer rate constants and initial distribution volume V_1 can be determined. Combining equation (A2.12) and (A2.13), using the boundary condition that $A_1(0) = N$, we obtain

$$V_1 = \frac{A_1(0)}{C_1(0)} = \frac{N}{a+b} \ . \tag{A2.14}$$

Combining equations (A2.1), (A2.13), and (A2.14):

$$\left.\frac{dA_1(t)}{dt}\right|_{t=0} = -(k_{10} + k_{12})N = -V_1(a\lambda_1 + b\lambda_2) \ \Leftrightarrow$$

$$\Leftrightarrow k_{10} + k_{12} = \frac{a\lambda_1 + b\lambda_2}{a+b}. \tag{A2.15}$$

From equation (A2.7), we note that

$$\lambda_1 + \lambda_2 = k_{10} + k_{21} + k_{12} \ , \tag{A2.16}$$

and that

$$\lambda_1\lambda_2 = k_{10}k_{21} \ . \tag{A2.17}$$

Inserting (A2.15) into (A2.16) and solving for k_{21} gives

$$k_{21} = \frac{a\lambda_2 + b\lambda_1}{a+b}. \tag{A2.18}$$

Inserting the expression for k_{21} in equation (A2.17) and solving for k_{10} yields

$$k_{10} = \frac{\lambda_1\lambda_2(a+b)}{a\lambda_2+b\lambda_1}. \tag{A2.19}$$

Using equation (A2.15), k_{12} is given by

$$k_{12} = \frac{a\lambda_1+b\lambda_2}{a+b} - k_{10} = \frac{ab(\lambda_1-\lambda_2)^2}{(a+b)(a\lambda_2+b\lambda_1)} \ . \tag{A2.20}$$

The compartmental clearance is the ratio between the irreversible elimination rate and the tracer concentration in the specific compartment. The central compartment clearance Cl_c is hence given by

$$Cl_c = \frac{A_1(t) \cdot k_{10}}{C_1(t)} = \frac{A_1(t) \cdot k_{10}}{A_1(t)/V_1} = V_1 \cdot k_{10}\,. \qquad \text{(A2.21)}$$

Inserting the expressions for V_1 from (A2.14) and k_{10} from (A2.19), the standard formula for bi-exponential plasma clearance calculations is obtained as:

$$Cl_c = \frac{N}{a+b} \cdot \frac{\lambda_1\lambda_2(a+b)}{a\lambda_2 + b\lambda_1} = \frac{N\lambda_1\lambda_2}{a\lambda_2 + b\lambda_1}, \qquad \text{(A2.22)}$$

which also can also be identified as the injected amount N divided by the integral of the plasma curve $C_1(t)$ from zero to infinity, since

$$Cl_c = \frac{N}{\int_0^\infty C_1(t)dt} = \frac{N}{\frac{a}{\lambda_1} + \frac{b}{\lambda_2}} = \frac{N\lambda_1\lambda_2}{a\lambda_2 + b\lambda_1}\,. \qquad \text{(A2.23)}$$

Printed by Media-Tryck, Lund 2017 NORDIC ECOLABEL. 3041 0903

LUND UNIVERSITY

Faculty of Science
Department of Medical Radiation Physics

ISBN 978-91-7753-385-6
ISBN 978-91-7753-386-3